

On the strength of the $U_A(1)$ anomaly at the chiral phase transition in $N_f = 2$ QCD

Bastian B. Brandt^{a,b}, Anthony Francis^c, Harvey B. Meyer^d, Owe Philipsen^a, Daniel Robaina^d, Hartmut Wittig^d

^a*Institut für Theoretische Physik, Goethe-Universität, D-60438 Frankfurt am Main*

^b*Institut für theoretische Physik, Universität Regensburg, D-93040 Regensburg*

^c*Department of Physics & Astronomy, York University, 4700 Keele St, Toronto, ON M3J 1P3, Canada*

^d*PRISMA Cluster of Excellence, Institut für Kernphysik and Helmholtz Institut Mainz, Johannes Gutenberg-Universität Mainz, D-55099 Mainz, Germany*

ABSTRACT: We study the thermal transition of QCD with two degenerate light flavours by lattice simulations using $O(a)$ -improved Wilson quarks. Temperature scans are performed at a fixed value of $N_t = (aT)^{-1} = 16$, where a is the lattice spacing and T the temperature, at three fixed zero-temperature pion masses between 200 MeV and 540 MeV. In this range we find that the transition is consistent with a broad crossover. As a probe of the restoration of chiral symmetry, we study the static screening spectrum. We observe a degeneracy between the transverse isovector vector and axial-vector channels starting from the transition temperature. Particularly striking is the strong reduction of the splitting between isovector scalar and pseudoscalar screening masses around the chiral phase transition by at least a factor of three compared to its value at zero temperature. In fact, the splitting is consistent with zero within our uncertainties. This disfavors a chiral phase transition in the $O(4)$ universality class.

Contents

1	Introduction	1
2	Lattice simulations	6
2.1	Simulation and scan setup	6
2.2	Scale setting and lines of constant physics	7
2.3	Observables and renormalisation	7
2.3.1	Deconfinement and the Polyakov loop	7
2.3.2	The chiral condensate	8
2.3.3	Mesonic correlation functions and screening masses	10
2.4	Investigating the order of the transition in the chiral limit	11
2.4.1	Critical scaling	11
2.4.2	$U_A(1)$ symmetry restoration	12
3	Results	13
3.1	Ensembles and measurement setup	13
3.2	The pseudocritical temperature	13
3.2.1	Polyakov loops	14
3.2.2	Chiral condensate and its susceptibility	15
3.2.3	Scaling in the approach to the chiral limit	16
3.3	Screening masses and chiral symmetry restoration pattern	19
3.4	On the relative size of the $U_A(1)$ breaking effects around T_C	25
4	Conclusions	27
A	Simulation and analysis details	29
A.1	Simulation algorithms and associated constraints	29
A.2	Error analysis	30
A.3	Interpolation of zero temperature quantities	30
A.4	Estimating lines of constant physics	31
A.5	Interpolation of the zero temperature chiral condensate	33
B	Simulation parameters and results	34

1 Introduction

Nuclear matter under extreme conditions of high temperatures T and/or baryon chemical potential μ_B is the subject of intense experimental and theoretical studies in nuclear, particle and astro-physics. One of the salient features of strongly interacting matter is

the high-temperature transition from the hadronic phase to the deconfined quark-gluon plasma (QGP). The transition takes place in a temperature regime between 100 and 300 MeV, where the QCD running coupling is strong. Thus, a non-perturbative investigation of the transition and the properties of the QGP is necessary and a lot of effort has been invested by the lattice community in the past decades (for recent reviews see [1–5]).

Because lattice studies of the QCD transition at finite baryon chemical potentials are severely hampered by the sign problem, the QCD phase diagram remains largely unknown. Even at zero baryon density, the nature of the thermal transition with light quark masses approaching the chiral limit is not yet determined in the continuum. Knowledge of this important limit would also help to constrain the phase diagram at non-zero μ_B . Fig. 1 summarises the current knowledge about the order of the thermal transition for vanishing baryon density in the (m_{ud}, m_s) -plane, where m_{ud} is the mass of the degenerate up and down quarks and m_s the strange quark mass. In the opposite limits of pure gauge theory and QCD with three massless quarks, there are true first-order phase transitions associated with the breaking of centre symmetry [6], and the restoration of the SU(3) chiral symmetry [7], respectively. These get weakened by the explicit breaking of those symmetries by finite fermion masses, until they disappear along second order critical lines. For intermediate quark masses, the finite temperature transition is then merely an analytic crossover.

There is plenty of evidence that the physical quark mass configuration realised in nature is in the crossover region. Early results based on the staggered fermion discretisation [8, 9] have been confirmed by domain wall fermions [10, 11] and simulations with Wilson fermions are approaching the physical point as well [12–15]. The critical line separating the first order chiral transitions from the crossover region, the chiral critical line, has been mapped out on coarse lattices and is in the Z(2) universality class of the 3d Ising model [16, 17]. The critical line in the heavy quark region, the deconfinement critical line, is in the same universality class and was mapped out on coarse lattices simulating a hopping expanded determinant [18] and a 3d effective lattice theory [19]. However, the location of the critical lines in the quark mass plane is subject to severe cut-off effects. With standard staggered fermions the $N_f = 3$ critical pion mass is at around two to three times the physical quark mass [16, 17], yet one finds that it shrinks to nearly half that value when going from $N_t = 4$ to $N_t = 6$ [20]. Improved staggered fermions can only give an upper bound for the critical mass which is around 0.1 times the physical quark mass [21, 22]. First results with Wilson fermions on the other hand see the $N_f = 3$ critical endpoint at around five times the physical quark mass [23]. While the latter result will still change when going towards finer lattices, it highlights the importance of taking the continuum limit before discussing critical behaviour.

While all current results indicate that the critical line passes the physical point to the left, its detailed continuation is still largely unknown [2]. There are two possible scenarios [7, 24, 25]: in scenario (1), depicted in the left panel of Fig. 1, the chiral critical line reaches the $m_{ud} = 0$ axis at some tri-critical point $m_s = m_s^{tric}$, implying a second order transition for $N_f = 2$. In the alternative scenario (2) the chiral critical line never reaches the $m_{ud} = 0$ axis, so that the chiral transition at $m_{ud} = 0$ is first order for all values of the strange quark mass.

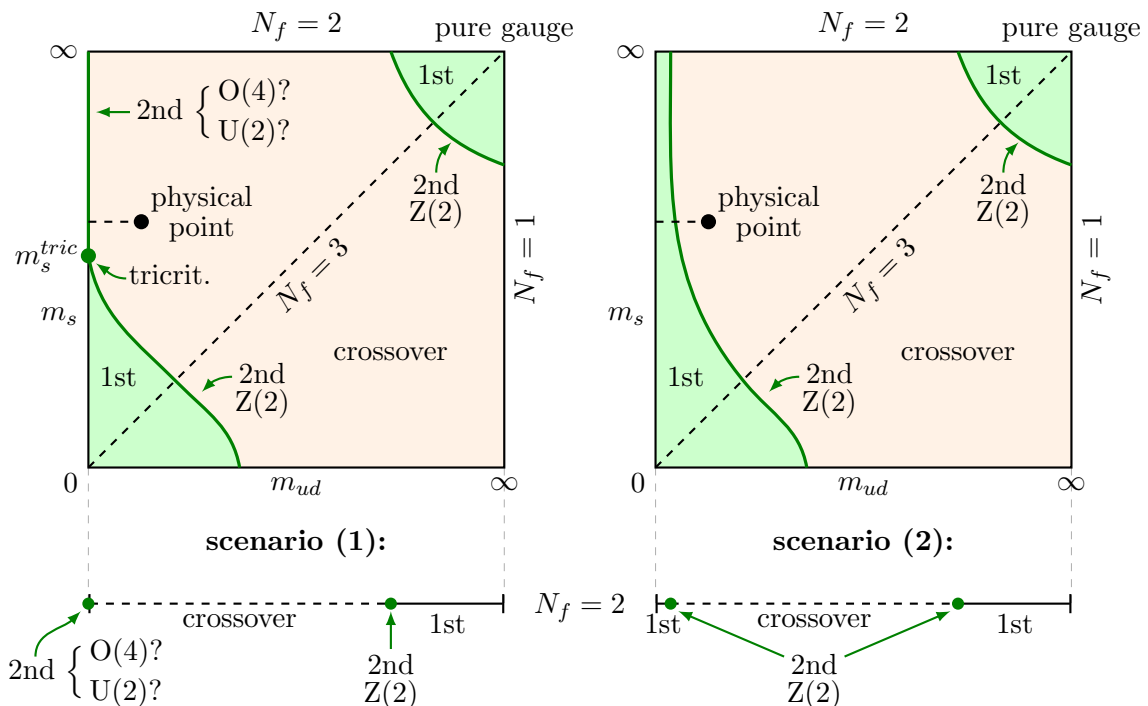


Figure 1. The two possible scenarios for the quark mass dependence of the phase structure of QCD at zero chemical potential. The lower lines highlight the dependence of the phase structure in the $N_f = 2$ case of the u and d quark masses.

Many past studies have investigated the nature of the $N_f = 2$ transition using staggered [26–32], $O(a)$ improved [33–35] or twisted mass [36] Wilson fermions and domain wall and overlap fermions [37–40], without being able to provide a conclusive answer in the chiral limit. The main problem in investigating scaling properties is the similarity of the critical exponents of the universality classes in question (cf. section 2.4.1). A new method to exploit the known tricritical scaling when coming from the plane of imaginary chemical potential has been proposed in [41]. First results on coarse lattices with staggered [42] and Wilson fermions [43] agree on scenario (2), but show enormous quantitative discrepancies. A similar approach proposed recently is to look at the extension of the chiral critical line in the plane with N_F additional degenerate heavy quarks [44, 45].

Which of these scenarios is realised depends crucially on the strength of the anomalous breaking of the $U_A(1)$ symmetry at the critical temperature in the chiral limit when the mass of the strange quark is sent to infinity, i.e. in the $N_f = 2$ case. If the breaking of $U_A(1)$ remains strong, the transition will be of second order in the $O(4)$ universality class [7], so that scenario (1) will be realised. If, on the other hand, the symmetry is ‘sufficiently’ restored (see the discussion below about different restoration criteria), either scenario is possible [24, 25]. For scenario (1) the breaking would then likely be in the $U(2) \times U(2) \rightarrow U(2)$ universality class [24, 25] (another symmetry breaking pattern/universality class of the form $SU(2) \times SU(2) \times Z_4 \rightarrow SU(2)$ has also been proposed [46, 47]) and the $O(4)$

universality class would be disfavoured. To be able to distinguish between the different scenarios by looking at the $U_A(1)$ symmetry, it is thus crucial to have a measure for the strength of the breaking.

First, we recall that the $U_A(1)$ classical symmetry does not imply the existence of a conserved current: the divergence of the singlet axial current $A_\mu^0(x)$ is proportional to the gluonic operator $G\tilde{G} = \epsilon_{\mu\nu\rho\sigma}G_{\mu\nu}G_{\rho\sigma}$ in the chiral limit, an equality valid in any on-shell correlation function. For instance, the static correlator $(\partial^2/\partial x_3^2) \int dx_0 dx_1 dx_2 \langle A_3^0(x) A_3^0(0) \rangle$ is proportional to the corresponding static two-point function of $G\tilde{G}$, which is certainly non-vanishing at any finite temperature. By contrast, the corresponding two-point function of the non-singlet axial current $A_3^a(x)$ vanishes in the chiral limit. In this particular sense, the $U_A(1)$ symmetry is never restored.

In this paper we use static correlators and the associated screening spectrum to probe the $U_A(1)$ effects. A thermal state with an exactly restored $U_A(1)$ symmetry implies that the correlators $\langle \bar{\psi}(x)\tau^a\psi(x)\bar{\psi}(0)\tau^a\psi(0) \rangle$ and $\langle \bar{\psi}(x)\gamma_5\tau^a\psi(x)\bar{\psi}(0)\gamma_5\tau^a\psi(0) \rangle$ are equal in the massless theory. However, we expect the restoration of $U_A(1)$ symmetry in this sense to only be partial, improving as the temperature is increased (see e.g. [48]).

In the literature, the restoration of $U_A(1)$ symmetry has also been discussed in a different, more restrictive sense. The observables considered are e.g. the correlation functions mentioned in the previous paragraph projected onto zero-momentum ($\int d^4x$). Similar to the Banks-Casher relation for the chiral condensate, the difference of the zero-momentum correlators can be expressed in terms of the spectral density of the Dirac operator alone [49, 50]. For a density $\rho(\lambda) \sim |\lambda|^\alpha$ with $\alpha > 1$, the difference vanishes exactly in the chiral limit. In such a scenario, it is said that $U_A(1)$ symmetry is restored. More generally, if the $SU(2)$ symmetry is restored at T_C (which we will find to be the case later), the effective restoration of the $U_A(1)$ symmetry is indicated by the degeneracy of correlation functions belonging to a $U(2) \times U(2)$ multiplet (e.g. [49]). Using the restoration of the $SU(2)$ symmetry, it was shown by Cohen [49, 50] that the degeneracy of zero-momentum correlation functions in the multiplets is directly linked to the eigenvalue density $\rho(\lambda)$ in the vicinity of zero. In particular, if the spectrum of the Dirac operator develops a gap around $\lambda = 0$ at T_C , the $U_A(1)$ symmetry becomes effectively restored. Using QCD inequalities, it has been argued that the $U_A(1)$ symmetry is expected to be effectively restored as soon as the $SU(2)$ symmetry is intact [49]. Later it was noted that the result using the inequalities was incorrect since the contributions from sectors with non-zero topology had not been taken into account properly [51, 52]. However, the non-zero topology sectors only contribute away from the thermodynamic limit. Only a bit later it was shown that the eigenvalue density in the chiral limit behaves like $\rho(\lambda) \sim |\lambda|^\alpha$ with $\alpha > 1$ [50]. Using mild assumptions and Ward-Takahashi identities for higher order susceptibilities in the framework of overlap fermions on the lattice, it has recently been shown that in fact $\alpha > 2$ [53], meaning that not only the eigenvalue density, but also its first and second derivative vanish at the origin, speaking strongly in favour of a restoration of the $U_A(1)$ symmetry.

The relation between degeneracy of correlators and the behaviour of the low modes of the Dirac operator triggered a number of numerical studies of the eigenvalue spectrum

in the vicinity of T_C [10, 37–40, 54]. Some groups [37, 38] see a restoration of $U_A(1)$ at T_C in the chiral limit (in particular, in [37] the behaviour of $\rho(\lambda) \sim |\lambda|^3$ was observed), while others claim that $U_A(1)$ will still be broken in the chiral limit [10, 54]. The difference between these studies is (apart from lattice spacings and volumes) the fermion action in use, in particular, how well the actions preserve chiral symmetry. In fact [53], to be able to show that the breaking of $U_A(1)$ still affects zero-momentum correlation functions via the low eigenvalues of the Dirac operator it is mandatory to fulfill the requirements of: (a) restored chiral symmetry on the lattice; (b) extrapolation to the infinite volume limit; (c) extrapolation to the chiral limit. In particular, condition (a) appears to play a crucial role. The reason is that any explicit breaking of the symmetry in the chiral limit by the lattice interferes with the effective restoration. Furthermore, it is mandatory to use the same fermion action also for the sea quarks, as shown in [39, 40]. Here the authors looked at the small eigenvalues with domain-wall fermions and overlap fermions on the domain-wall ensembles and observed a broken $U_A(1)$ symmetry, actually made worse by the use of “quenched” overlap quarks. Only after reweighting of the configurations to the overlap ensemble an actual restoration of $U_A(1)$ in the chiral limit was observed. A possible explanation for this effect is that the “quenching” of the overlap operator leads to the appearance of non-physical near zero modes in the overlap spectrum, much like the appearance of exceptional configurations in quenched QCD. Indeed, the cases where a residual breaking was observed were those where either or both, valence and sea quarks, might not have a fully restored chiral symmetry on the lattice. Similar conclusions have been found using chiral susceptibilities, which can also be related to the eigenvalue spectrum, e.g. [10, 40, 55]. However, when computed on the lattice, the susceptibilities suffer from contact terms, which need to be carefully subtracted to obtain conclusive results.

In this article we present a study of the phase transition in two-flavour QCD using non-perturbatively $O(a)$ improved Wilson fermions [56] and the Wilson plaquette action [57]. We work with a large temporal lattice extent of $N_t = 16$ throughout, which at the chiral transition corresponds to a lattice spacing $a \approx 0.07$ to 0.08 fm. Our pion masses range from about 200 to 500 MeV. In particular, we study the pseudo-critical temperatures defined by the change in the Polyakov loop and the chiral condensate, pertaining to deconfinement and chiral symmetry restoration, respectively, and check for the associated scaling in the approach to the chiral limit. As already discussed in [58], such a scaling analysis is not sufficient to distinguish between the universality classes in question. We thus direct our attention to the strength of the $U_A(1)$ breaking by investigating the degeneracy pattern of screening masses. This is complementary to other studies of the $U_A(1)$ symmetry in the literature described above, e.g. [10, 11, 38–40], which are based on the eigenvalue structure of the Dirac operator. The screening masses probe the long-distance properties the correlators and are free of contaminations from contact terms, unlike chiral susceptibilities. We propose a measure for the strength of the $U_A(1)$ -breaking in the vicinity of T_C and extrapolate it to the chiral limit. There we find it to be consistent with zero and 3 standard deviations away from its non-zero value at zero temperature. This suggests an effective restoration of the $U_A(1)$ symmetry around the critical temperature and thus a strengthening of the chiral transition for the lattice spacing considered.

As discussed above, at finite lattice spacing an exact chiral symmetry is mandatory in order to study the eigenvalue spectrum of the Dirac operator reliably. In this study we use $O(a)$ improved Wilson fermions. While the action breaks chiral symmetry at finite lattice spacing, the static screening masses that we study approach their continuum limit with $O(a^2)$ corrections. Therefore, as long as we work in a regime where these corrections are small compared to the physical mass splittings induced by the $U_A(1)$ anomaly, we should obtain qualitatively correct conclusions. If, at a given lattice spacing, a $U_A(1)$ -breaking mass splitting turns out to be small, a continuum extrapolation is required to determine how small exactly the splitting is.

Parts of our results have already been presented at conferences [58–61] and were used to investigate the properties of the pion quasiparticle in the vicinity of the transition [62–65].

The article is organised as follows: In the next section we introduce our observables, the details of our simulations and discuss the renormalisation and scale-setting procedures. In section 3, we present the numerical results. We first discuss the extraction of the pseudo-critical temperatures in section 3.2 and try to compare the results to the scaling predictions in the approach to the chiral limit. We also compare our results with those from different fermion discretisations in the literature. In section 3.3 we discuss the screening masses in the different channels, before we come to the investigation of the strength of the breaking in the chiral limit in section 3.4. Finally we present our conclusions in section 4. Detailed tables collecting simulations parameters and results can be found in the appendices.

2 Lattice simulations

2.1 Simulation and scan setup

Our simulations are performed using two flavours of non-perturbatively $O(a)$ improved Wilson fermions [56] and the unimproved Wilson plaquette action [57]. We use the clover coefficient determined non-perturbatively in Ref. [66]. The simulations are done employing deflation accelerated versions of the Schwarz [67, 68] (DD) and mass [69] (MP) preconditioned algorithms, the latter in the implementation of Ref. [70]. Both algorithms make use of the Schwarz preconditioned and deflation accelerated solver introduced in [71, 72]. As discussed in detail appendix A.1, the algorithms offer a significant speedup for large volumes and low quark masses, but also pose constraints on the available lattice sizes.

In general there are two known procedures to vary the temperature $T = 1/(N_t a)$. The first option is to vary the temporal extent whilst keeping the lattice spacing fixed. The advantage of this procedure is that all physical parameters and renormalisation constants remain fixed, making it the optimal tool for spectroscopy (see [73], for instance). The disadvantage of this procedure is that the resolution around T_C is limited, made even worse by the use of improved algorithms (cf. appendix A.1). The second option, used in this study, is to vary the lattice spacing a by varying the coupling $\beta = 6/g_0^2$, known as β -scans. This offers the possibility to obtain a fine resolution around T_C , but requires a good tuning of the bare quark mass to scan along lines of constant physics (LCPs), as well as the interpolation of quantities needed for scale setting and renormalisation. This is particularly demanding for Wilson fermions due to the additive quark mass renormalisation.

We will use throughout a comparatively large temporal extent of $N_t = 16$ for two reasons. First, Wilson fermions break chiral symmetry explicitly at finite lattice spacing. Being as close as possible to the continuum helps to reduce the resulting effects as much as possible. Second, for our choice of lattice action the non-perturbative determination of the improvement coefficient c_{SW} in the two-flavour theory extends only down to $\beta = 5.2$ [74]. Since $a \approx 0.08$ fm at $\beta = 5.2$ this means that $N_t = 16$ is necessary to allow for scans in the desired temperature range.

2.2 Scale setting and lines of constant physics

To convert our results to physical units we use the Sommer scale [75] r_0 with the interpolation of the CLS results from [74] discussed in appendix A.3. To convert to physical units we use the continuum result $r_0 = 0.503(10)$ fm [74]. The temperature scans are done along LCPs, for which we estimate the values for the bare parameter κ corresponding to a particular quark mass by inverting the analytic relation $m_{ud}(\beta, \kappa)$ discussed in appendix A.4. We test the validity of this relation a posteriori by computing m_{ud} along the β -scan. Conventionally, quark masses will be quoted in the $\overline{\text{MS}}$ scheme at a renormalisation scale of 2 GeV.

Whenever we quote pion masses for our temperature scans, we imply that these are zero temperature pion masses which correspond to the quark masses of the respective ensemble. We estimate the pion masses from our results for m_{ud} using chiral perturbation theory to next-to-next-to leading order as given in [76]. For this we use the low-energy constants from [77] obtained by the fit denoted as ‘NNLO F_π, m_π^2 ’ with a mass cut of 560 MeV. The associated low-energy constants are given in table 6 of [77]. This procedure serves the purpose of enabling comparisons with the literature and should not be taken as a precision computation of the zero temperature pion mass.

2.3 Observables and renormalisation

2.3.1 Deconfinement and the Polyakov loop

To investigate the deconfinement properties of the transition we look at the associated order parameter, the Polyakov loop

$$L = \frac{1}{V} \sum_{\vec{x}} \text{Tr} \left\{ \prod_{n_0=1}^{N_t} U_0(n_0 a, \vec{x}) \right\}, \quad (2.1)$$

a nonzero value of which signals the spontaneous breaking of centre symmetry. Dynamical fermions explicitly break the centre symmetry of the gauge action and favour the centre sector of the Polyakov loop on the real axis, so that it is sufficient to look at $\langle \text{Re}(L) \rangle$. In [78] it was found that the use of smeared links can enhance the signal in investigations of phase transitions. We have thus also computed the real part of the APE-smeared [79] Polyakov loop, $\langle \text{Re}(L)_S \rangle$, using 5 steps of APE smearing with a parameter of 0.5 multiplying the staples. The Polyakov loop susceptibility is given by

$$\chi_L = V \left(\langle \text{Re}(L)^2 \rangle - \langle \text{Re}(L) \rangle^2 \right) \quad (2.2)$$

and similarly for the smeared Polyakov loop. In order to have a quantity with a well defined continuum limit the Polyakov loop requires multiplicative renormalisation [80]. Here we will ignore this issue and work with the unrenormalised Polyakov loop. Since the renormalisation factor is expected to behave monotonically at the β values corresponding to the critical region, we do not expect the typical S-shape of the Polyakov loop vs. temperature graph to be affected.

2.3.2 The chiral condensate

A second aspect of the transition to the quark gluon plasma is the restoration of chiral symmetry. In the chiral limit, the associated order parameter is the chiral condensate

$$\langle \bar{\psi}\psi \rangle = -\frac{T}{V} \frac{\partial \ln(Z)}{\partial m_{ud}}. \quad (2.3)$$

It governs the response of the system with respect to the external ‘field’ which breaks the symmetry explicitly, i.e., the quark mass m_{ud} . The bare chiral condensate is given by

$$\langle \bar{\psi}\psi \rangle^{\text{bare}} = -\frac{N_f T}{V} \langle \text{Tr}(D^{-1}) \rangle_U, \quad (2.4)$$

where D is the Dirac operator and the expectation value on the right-hand side is taken with respect to the gauge field.

The associated susceptibility

$$\chi_{\langle \bar{\psi}\psi \rangle} = \frac{T}{V} \frac{\partial^2 \ln(Z)}{\partial m_{ud}^2} \quad (2.5)$$

consists of a disconnected (the terms in the curly brackets) and a connected part,

$$\begin{aligned} \chi_{\langle \bar{\psi}\psi \rangle}^{\text{bare}} &= \frac{TN_f}{V} \left[\left\{ \langle \text{Tr}(D^{-1})^2 \rangle_U - \langle \text{Tr}(D^{-1}) \rangle_U^2 \right\} - \frac{1}{2} \langle \text{Tr}(D^{-1}D^{-1}) \rangle_U \right] \\ &= \chi_{\langle \bar{\psi}\psi \rangle}^{\text{bare}}|_{\text{disc}} - \frac{TN_f}{2V} \langle \text{Tr}(D^{-1}D^{-1}) \rangle_U. \end{aligned} \quad (2.6)$$

In the region around T_c the disconnected part has been found to dominate the transition signal in the susceptibility [9, 30, 81]. Close to the chiral limit, however, this statement does not necessarily hold. The connected part only receives contributions from isovector states, while the disconnected part receives contributions both from isovector and isoscalar states. Since an unbroken $U_A(1)$ symmetry would imply light isovector scalar states, the relevant magnitude of the two contributions is an important indicator of the nature of the transition. Here we will focus on the disconnected part of the susceptibility and leave the comparison between the connected and the disconnected susceptibility for future publications.

Due to mixings with operators of lower dimension, the condensate contains cubic, quadratic and linear divergences, and therefore requires additive renormalisation [82, 83]. In addition, it renormalises multiplicatively with the renormalisation factor associated with the scalar density, Z_S , which is equivalent to the inverse of the mass renormalisation factor for Wilson fermions, $Z_S = Z_m^{-1}$ [84], where Z_m is defined in appendix A.4. Neither the

additive nor the multiplicative renormalisation depends on the temperature, so that we can cancel the divergent terms by subtracting the chiral condensate at $T = 0$. The associated difference renormalises multiplicatively,

$$\langle \bar{\psi}\psi \rangle^{\text{ren}}(T) = Z_m^{-1} \left[\langle \bar{\psi}\psi \rangle^{\text{bare}}(T) - \langle \bar{\psi}\psi \rangle^{\text{bare}}(0) \right]. \quad (2.7)$$

For the determination of Z_m we can use eqs. (A.5), (A.6) and (A.7) to obtain

$$Z_m = \frac{Z_A}{Z_P} Z_{\text{PCAC}}(\beta)(1 + b_m a\bar{m}), \quad (2.8)$$

which is correct up to $O(a^2)$. $Z_{\text{PCAC}}(\beta)$ can be taken from the fit in appendix A.4.

Using axial Ward identities (AWIs) one can also define an observable which is free of cubic divergences and reproduces the chiral condensate in the chiral limit [83, 84]. The axial Ward identity in the form integrated over spacetime (and up to a contact term at $y = x$) is given by

$$\frac{1}{N_f} \left[\langle \bar{\psi}\psi \rangle^{\text{bare}}(x) - b_0 \right] = 2m_{\text{PCAC}} a^4 \sum_y \langle P(x)P(y) \rangle - Z_A a^4 \sum_y \partial_y^\mu \langle P(x)A_\mu(y) \rangle, \quad (2.9)$$

where m_{PCAC} is the bare PCAC quark mass and b_0 represents the cubic divergence in the bare condensate. At finite quark mass the second term on the r.h.s. vanishes due to the absence of a true Goldstone boson [84] and we can use the first term as the definition of a bare subtracted condensate

$$\langle \bar{\psi}\psi \rangle_{\text{sub}}^{\text{bare}} = 2N_f m_{\text{PCAC}} \langle \overline{PP} \rangle \quad (2.10)$$

with

$$\overline{PP} = \frac{a^4}{N_t N_s^3} \sum_{x,y} P(x)P(y) = \frac{T}{V} \text{Tr}(D^{-1}\gamma_5 D^{-1}\gamma_5). \quad (2.11)$$

$\langle \bar{\psi}\psi \rangle_{\text{sub}}^{\text{bare}}$ still suffers from additive quadratic and linear divergences and renormalises multiplicatively with Z_P [84]. Again we can subtract the residual additive divergences using the $T = 0$ counterpart, so that we obtain an alternative renormalised chiral condensate

$$\langle \bar{\psi}\psi \rangle_{\text{sub}}^{\text{ren}}(T) = Z_P \left[\langle \bar{\psi}\psi \rangle_{\text{sub}}^{\text{bare}}(T) - \langle \bar{\psi}\psi \rangle_{\text{sub}}^{\text{bare}}(0) \right]. \quad (2.12)$$

We define the susceptibility of the quantity (2.10) as

$$\bar{\chi}_{\langle \bar{\psi}\psi \rangle_{\text{sub}}^{\text{bare}}} = 4N_f^2 V m_{\text{PCAC}}^2 \left[\langle \overline{PP^2} \rangle - \langle \overline{PP} \rangle^2 \right]. \quad (2.13)$$

Note that, while $\bar{\chi}_{\langle \bar{\psi}\psi \rangle_{\text{sub}}^{\text{bare}}}$ is not equivalent to the disconnected chiral susceptibility in eq. (2.6), it is expected to show a peak at the position of the chiral transition. The subtraction of the condensates at $T = 0$ requires the measurement of $\langle \bar{\psi}\psi \rangle^{\text{bare}}$ and $\langle \overline{PP} \rangle$ on zero temperature ensembles. Here we use the set of $N_f = 2$ ensembles generated within the CLS effort and the interpolation discussed in appendix A.5.

channel	S	P	V	A
Γ	$\mathbf{1}$	γ_5	γ_i	$\gamma_i\gamma_5$

Table 1. Bilinear operators $\bar{\psi}\Gamma\psi$ used for the screening correlators. Here $i = 1, 2$ for screening masses in x^3 -direction.

2.3.3 Mesonic correlation functions and screening masses

Mesonic correlation functions are a valuable probe of the properties of the QGP [85, 86]. Let

$$C_{XY}(x_\mu) = \int d^3x_\perp \langle X(x_\mu, \mathbf{x}_\perp) Y(0) \rangle, \quad (2.14)$$

be the correlation function of two operators X and Y . The equality of two correlation functions in channels of different quantum numbers signals the restoration of the associated chiral symmetry. Here x_μ is the coordinate of the direction in which the correlation function is evaluated and \mathbf{x}_\perp is the coordinate vector in the orthogonal subspace. The isovector correlation functions of interest for the chiral transition are the vector (V) vs. axial-vector (A), and the pseudoscalar (P) vs. scalar (S) channels, related by

$$C_{VV} \xleftrightarrow{\text{SU}(2)} C_{AA} \quad \text{and} \quad C_{PP} \xleftrightarrow{\text{U}_A(1)} C_{SS}. \quad (2.15)$$

We choose the isovector channels as observables because they are free of disconnected diagrams, and the correlation functions can therefore be obtained with greater accuracy. The bilinear operators for the different channels are listed in table 1.

While temporal correlation functions $C_{XY}(x_0)$ can be related to the real-time spectral densities (see [87]), here we are interested in spatial correlation functions $C_{XY}(x_3)$, which are related to the screening states of the plasma. In particular, the leading exponential decay of the correlator $C_{XX}(x_3)$ defines the lowest-lying ‘screening mass’ M_X associated with the quantum numbers of the operator X . Screening masses can be interpreted as the inverse length scale over which a perturbation is screened by the plasma. If a symmetry imposes the equality of two correlation functions, it must also imply the degeneracy of the corresponding screening masses. The latter are thus quantities sensitive to the restoration of the symmetry. Consequently, the screening masses in the V and A channels provide an alternative way of defining the chiral symmetry restoration temperature. In contrast to susceptibilities, defined by the integrated correlation function, screening masses probe the long-distance properties of the correlation functions and thus do not suffer from contact terms.

Apart from their relation to chiral symmetry, mesonic screening masses are valuable quantities to probe the medium effects of the plasma and, at high temperatures, to test the applicability of perturbation theory. They have been studied in lattice QCD for a long time (for a review of early results see [88] and for more recent studies [89, 90]). In the high-temperature limit, all screening masses approach the asymptotic value $M^\infty = 2\pi T$ [91, 92]. The leading order correction from the interactions has been computed in perturbation theory and is known to be positive [93, 94]. Static and non-static screening masses can

also be computed within an effective theory approach and provide an indirect probe for real-time physics in the Euclidean lattice setup [95, 96].

2.4 Investigating the order of the transition in the chiral limit

2.4.1 Critical scaling

The main question driving the present study is the nature of the phase transition in the chiral limit. Simulations with vanishing quark masses are currently impossible; in order to extract information on the order of the transition, it is customary to investigate the scaling of various observables in the approach to the critical point $(0, 0)$ in the parameter space of reduced temperature $\tau = (T - T_c)/T_c$ and external field h . The scaling laws can be derived from the scaling of the free energy F (see [97]). The variable playing the role of the external field depends on the particular scenario (see section 1). If the second order scenario (scenario (1)) is realised, no matter whether the universality class is $O(4)$ or the one from the $U(2) \times U(2) \rightarrow U(2)$ scenario¹, the critical point is located in the chiral limit and the chiral condensate constitutes a true order parameter. In this case the external field h is proportional to the (renormalised) quark mass m_{ud} . In the first-order scenario, depicted in the right panel of figure 1, the critical point is located at a finite quark mass m_{ud}^{cr} , so that chiral symmetry is broken explicitly at the critical point. One must in general expect that the external field is given by a linear combination of $\delta m = m_{ud} - m_{ud}^{\text{cr}}$ and τ . Furthermore, $\langle \bar{\psi}\psi \rangle$ no longer constitutes a true order parameter. The situation is analogous to the approach of the chiral critical line along the $N_f = 3$ axis [16].

Here we will perform an analysis based on the scaling of the order parameter or the transition temperature T_C with the external field. In the vicinity of the critical point a true order parameter Θ satisfies the scaling relation (see e.g. [9, 33, 97, 98])

$$\Theta \sim h^{1/\delta} f\left(\frac{\tau}{h^{1/(\delta\beta)}}\right) + \text{s.v.} \quad (2.16)$$

Here f is a function depending on the universality class of the transition and s.v. stands for scaling violations which constitute terms that are regular in τ [9, 97, 98]. A number of studies have looked at the scaling of the chiral condensate in the approach to the chiral limit [9, 30, 33, 36, 98] and found consistency with $O(4)$ scaling.

From the scaling in eq. (2.16) one can also derive a scaling law for the critical temperature as a function of the external field [26]. The resulting scaling relation is

$$T_C(h) = T_C(0) \left[1 + Ch^{1/(\delta\beta)} \right] + \text{s.v.}, \quad (2.17)$$

where C is an unknown constant. It must be stressed that these scaling laws are only valid after the thermodynamic and continuum limits have been taken.

Another problem for any study of the scaling laws is the similarity of the critical exponents in the three potentially relevant universality classes. They are summarised in table 2. For the different scenarios the combination $\delta\beta$ is given by ≈ 1.56 for $Z(2)$, ≈ 1.86 for $O(4)$ and ≈ 1.85 for $U(2)$. Even between the $Z(2)$ and the $O(4)$ scenarios the difference

¹We will denote the $U(2) \times U(2) \rightarrow U(2)$ scenario in short as the $U(2)$ scenario from now on.

UC	ν	γ	β	δ	Ref.
Z(2)	0.6301(4)	1.2372(5)	0.3265(3)	4.789(2)	[97]
O(4)	0.7479(90)	1.477 (18)	0.3836(46)	4.851(22)	[99]
U(2)	0.76(10)(5)	1.4(2)(1)	0.42(6)(2)	4.4(3)(1)	[25]

Table 2. Critical exponents for the universality classes (UC) relevant for the chiral transition. The critical exponents of the $U(2)\times U(2)\rightarrow U(2)$ universality class, we have taken the results from [25] (from the \overline{MS} scheme). The first error is statistical while the second quoted error denotes a systematic uncertainty arising from the scheme dependence. The critical exponents of the $U(2)\times U(2)\rightarrow U(2)$ universality class have also been obtained recently using the bootstrap method [100].

is so small that very accurate results are needed to be able to distinguish between the two. Thus one cannot draw conclusions from the agreement of lattice data with the scaling of one universality class alone; instead one needs to demonstrate the ability to distinguish between the scenarios.

2.4.2 $U_A(1)$ symmetry restoration

The strength of the anomalous breaking of the $U_A(1)$ symmetry at the transition temperature in the chiral limit is thought to be crucial for the order of the chiral transition [7, 101]. However, this raises the question of how to quantify the strength of the $U_A(1)$ -breaking. As a possible reference value we suggest the screening mass gap between the isovector pseudoscalar and scalar channels at $T = 0$,

$$\Delta M_{PS} = M_P - M_S = -m_{a_0}, \quad (2.18)$$

since the pion mass vanishes in the chiral limit. Ultimately, one would like to obtain the chirally extrapolated value of m_{a_0} from lattice QCD, since this would give a result valid for the $N_f = 2$ case in the range of relevant lattice spacings. Unfortunately, the scalar correlation function in the iso-vector channel is rather noisy, so that a reliable extraction is currently not possible. We will discuss a phenomenological estimate for the chiral limit in section 3.4.

We note that in the two-flavour theory, the a_0 meson is expected to be stable or almost stable, since the $\bar{K}K$ and $\eta\pi$ decay channels known from experiment are missing. Indeed, in $N_f = 2$ QCD only a flavour-singlet pseudoscalar exists, sometimes called η_2 , whose nature is closer to the physical η' meson, and whose mass has been estimated at about 800MeV at the physical pion mass [102]. The lightest isovector scalar state was found to lie between the physical $a_0(980)$ and $a_0(1450)$ states [103]. The splitting between the pion and the lightest isovector scalar state thus provides a convenient measure for the breaking of $U_A(1)$.

scan	Lattice	Algorithm	κ/m_{ud} [MeV]	m_π [MeV]	T [MeV]	τ_{UP} [MDU]	MDUs
B1 _{κ}	16×32^3	DD-HMC	0.136500		190 – 275	~ 20	~ 20000
C1	16×32^3	DD-HMC	~ 17.5	300	150 – 250	~ 28	~ 12000
D1	16×32^3	MP-HMC	~ 8.7	220	150 – 250	~ 16	~ 12000

Table 3. β -scans at $N_t = 16$. Listed is the temperature range in MeV, the integrated autocorrelation time of the plaquette τ_{UP} and the number of molecular dynamics units (MDUs) used for the analysis. For scan **B1** _{κ} configurations have been saved each 200 MDUs, for scan **C1** each 40 MDUs and for scan **D1** each 20 MDUs. The measurements of the Polyakov loop and the chiral condensate have been done each 4 MDUs. The autocorrelation times and numbers of measurements quoted here correspond to the ones at the location of the transition.

3 Results

3.1 Ensembles and measurement setup

In this paper we present results for the chiral transition obtained from the scans on 16×32^3 (and first results from 16×48^3) lattices summarised in table 3. More details can be found in table 10 in appendix B. We consider three different values of the quark mass, corresponding to pion masses between 200 to 540 MeV. The scan corresponding to the largest pion mass at the critical point, denoted as scan **B1** (in our naming convention the letter labels quark/pion masses while the number labels volumes), has been done at fixed hopping parameter, indicated by the subscript κ . Due to renormalisation and the change in the scale, the quark mass changes with the temperature in this scan. The scans at lighter quark masses, scans **C1** and **D1** with $m_\pi \approx 300$ and 220 MeV, are done along LCPs. To check the tuning of the quark masses we have measured the renormalised PCAC quark mass using the PCAC relation evaluated in the $x_3 \equiv z$ -direction (see [104]). The simulation points in the (T, m_{ud}) parameter space are shown in figure 2. The plot shows that the tuning of the quark mass works well in the region below T_C , while we see that we get smaller quark masses than expected above T_C . It is unclear to us whether this is a cutoff effect or if our interpolation just becomes worse in this region (cf. appendix A.4).

The quantities relevant for the transition temperature, i.e. the Polyakov loop and the chiral condensate, have been measured during the generation of the configurations with a separation of 4 MDUs. For the measurement of the condensate we have used 4 hits with a $Z_2 \times Z_2$ volume source. The exception is the **B1** _{κ} scan, where the chiral condensate has only been measured on the stored configurations, using 100 hits. The screening masses have been measured on the stored configurations. For scan **B1** _{κ} , configurations have been saved every 200 MDUs, for scan **C1** every 40 MDUs and for scan **D1** every 20 MDUs. The results for the expectation values of Polyakov loops, the chiral condensates and screening masses are tabulated in tables 11 and 12 in appendix B.

3.2 The pseudocritical temperature

The first step of our investigation of the thermodynamics of QCD is the extraction of the pseudocritical temperatures. Since we are dealing with a crossover rather than a true phase

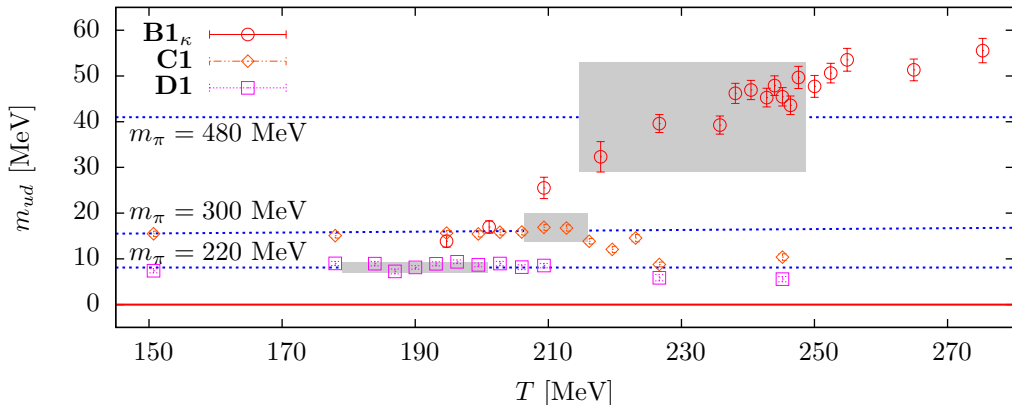


Figure 2. Simulation points in the $\{m_{ud}, T\}$ parameter space. The grey areas mark the estimates for the crossover regions.

transition there is no unique definition of the critical temperature and estimates for T_C will depend on the defining observable. To determine T_C we will primarily look at the Polyakov loop and the chiral condensate. In particular, the inflection point of the Polyakov loop will define the deconfinement transition temperature T_C^{dc} , while the peak in the susceptibility of the chiral condensate defines the temperature of chiral symmetry restoration, which will be our main estimate for T_C .

3.2.1 Polyakov loops

We start with the extraction of T_C^{dc} using the (unrenormalised) smeared Polyakov loop. We use $\langle \text{Re}(L)_S \rangle$ since it typically shows stronger signals for the transition. We have, however, checked the agreement with the results for the unsmeared Polyakov loop explicitly (see also [59]). The results are shown in figure 3. The observable $\langle \text{Re}(L)_S \rangle$ in scans **C1** and **D1** develops the S-shape characteristic for a phase transition, with some fluctuations in the vicinity of the inflection point. For scan **B1 $_{\kappa}$** the S-shape is not as prominent, possibly due to the limited temperature range explored. To extract the inflection point we have fitted $\langle \text{Re}(L)_S \rangle$ to the form of an arctangent. To check the model dependence of the results we have performed alternative fits using the Gaussian error function. Both fits tend to describe the data reasonably well and give similar χ^2/dof values. The resulting curves from the arctangent fits are shown as black lines in figure 3. The results for the associated transition temperatures T_C^{dc} are given in table 4. Evidently the estimate for the uncertainty of the inflection point from the fit cannot be reliable due to the strong fluctuations in its vicinity. To account for this additional uncertainty we have assigned another systematic error of 10 MeV to the result from the fit, reflecting the size of the interval where we observe deviations from the smooth behaviour of the Polyakov loop. The shaded areas in figure 3 represent the estimates for the transition region. In the vicinity of T_C^{dc} the Polyakov loop susceptibility increases and shows fluctuations that can be interpreted as the onset of peak-like behaviour. Owing to this typical behaviour, we suspect that T_C^{dc}

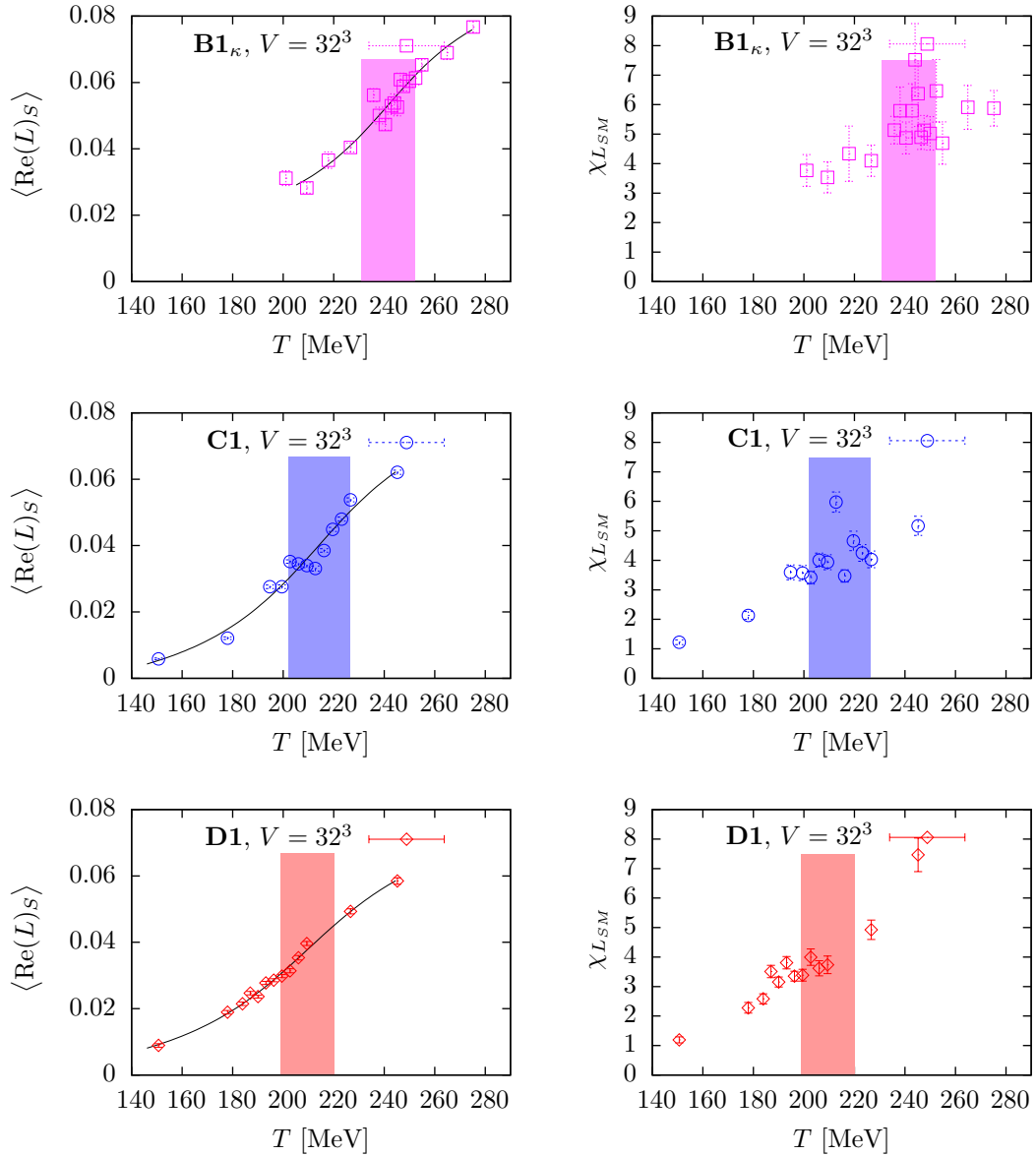


Figure 3. Results for the (unrenormalised) APE smeared Polyakov loop (left) and its susceptibility (right) for scans $\mathbf{B1}_\kappa$, $\mathbf{C1}$ and $\mathbf{D1}$ (from top to bottom). The shaded areas indicate the estimates for the transition regions and the black lines are the results from the fit of the Polyakov loop expectation value to the arctangent form.

could be somewhat overestimated for scan $\mathbf{D1}$.

3.2.2 Chiral condensate and its susceptibility

To estimate the chiral symmetry restoration temperatures, T_C , we use the renormalised disconnected susceptibility, of the chiral condensate without $T = 0$ subtractions. In particular, we have $Z_m^2 \chi_{(\psi\psi)}^{\text{bare}}|_{\text{disc}}$ and $Z_P^2 \bar{\chi}_{(\psi\psi)}^{\text{bare}}|_{\text{sub}}$ for condensate and subtracted condensate, respectively. Note that the additive renormalisation discussed in section 2.3.2 has not been

scan	T_C^{dc} [MeV]	T_C [MeV]	m_{ud}^C [MeV]	m_π^C [MeV]
B1$_\kappa$	241(5)(6)(10)	232(18)(6)	41 (11)(2)	485(55)(20)
C1	214(9)(3)(10)	211(5)(3)	16.8(30)(7)	300(27)(9)
D1	210(6)(3)(10)	190(10)(5)	8.1(12)(4)	214(14)(8)

Table 4. Results for the pseudocritical deconfinement, T_C^{dc} , and chiral symmetry restoration, T_C , temperatures and the associated critical value of the quark mass with its zero-temperature pion mass pendant. The first error reflects the uncertainty of the extraction of the pseudocritical temperatures due to the fit, the second error accounts for scale setting (and renormalisation). For T_C^{dc} the third error is the associated systematic error as explained in the text.

taken into account. However, the position of the peak in the susceptibility should not be affected, since the additive renormalisation gives regular contributions around T_C .

Figure 4 displays the results for the disconnected susceptibilities for the unsubtracted and subtracted bare condensates. We define the pseudocritical temperature for chiral symmetry restoration through the position of the peak in the susceptibility of the subtracted condensate. To determine T_C we fit the susceptibility to a Gaussian. Since the error estimate for T_C from the fit will likely underestimate the true uncertainty we take the full spread of points included in the fit as a conservative error estimate. The resulting values for T_C are given in table 4 and are shown as shaded areas in figure 4. The black curves correspond to the fit. Scan **B1 $_\kappa$** is a problematic case, since, due to the change of the quark mass, the scan remains longer in the vicinity of the critical region, $T_C(m_{ud})$. Consequently, the peak is broad and we obtain large uncertainties for both, T_C and m_{ud}^C . Comparing the results for T_C^{dc} with T_C , we see that they mostly agree within errors. The exception is **D1**, where we find that T_C^{dc} lies somewhat above T_C . Like other studies in the literature we see that T_C decreases with the quark mass [26–36], which is a general feature, persisting even when dynamical heavy quarks are included (e.g. [14, 15]).

In figure 5 we show the results for the fully renormalised condensate and the fully renormalised subtracted version for scans **C1** and **D1**. As expected, the condensates start close to zero and show a rapid decrease in the approach to T_C . Around T_C both condensates show fluctuations, especially the standard condensate fluctuates quite strongly. We note that T_C , as defined by the inflection point of the renormalised condensate, does not necessarily have to agree with the peak of the susceptibility for a broad crossover.

We also have preliminary data for the condensates from simulations on 16×48^3 lattices. These were mainly used to check finite size effects on the screening masses below and are insufficient for a precise finite size scaling analysis. However, they are fully consistent with saturating susceptibilities and a crossover, as expected.

3.2.3 Scaling in the approach to the chiral limit

Following section 2.4.1 we will now try to extract information about the order of the transition in the chiral limit by looking at the scaling of the temperatures with the quark mass. With three transition temperatures at our disposal and their relatively large uncertainties we are not in the position to extract the critical exponents from a fit of the data for T_C .

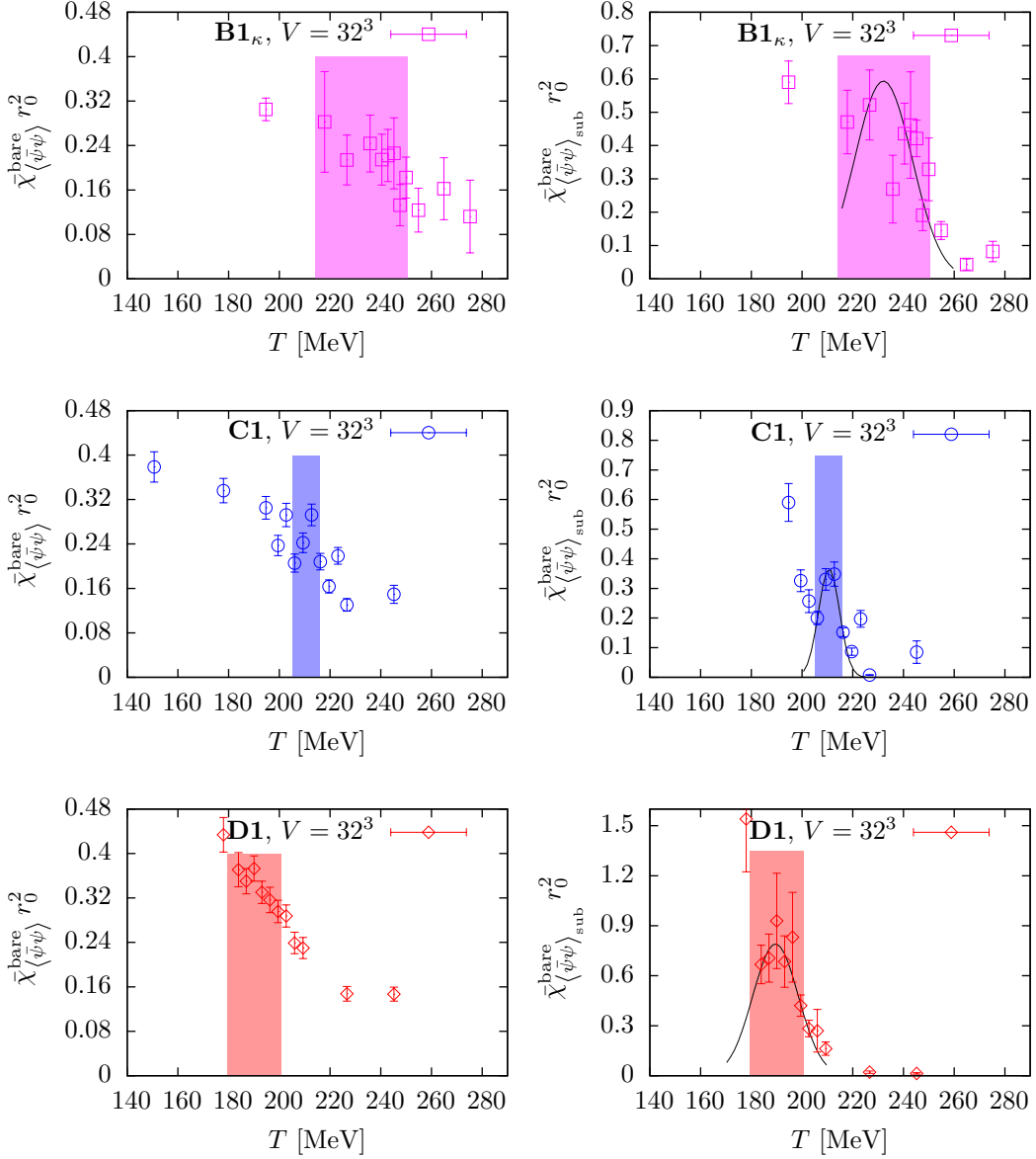


Figure 4. Results for the disconnected susceptibility of the condensate (left) and the subtracted condensate (right) for scans $\mathbf{B1}_\kappa$, $\mathbf{C1}$ and $\mathbf{D1}$ (from top to bottom). The shaded areas indicate the estimates for the transition regions and the black lines are the results from the fit of the susceptibility to a Gaussian.

Instead, we fix the critical exponents to the ones from the different universality classes and check whether any particular scenario is favoured by our data. We start by fitting the results for T_C from table 4 to eq. (2.17) with the critical exponents from the O(4) and U(2) scenarios. The results are shown in figure 6. The plot highlights the similarity of the two curves, indicating that the scaling of the transition temperatures alone will not be sufficient to distinguish between the two scenarios. We note that this is likely to remain true even when the error bars are reduced by an order of magnitude. Potentially, a scaling

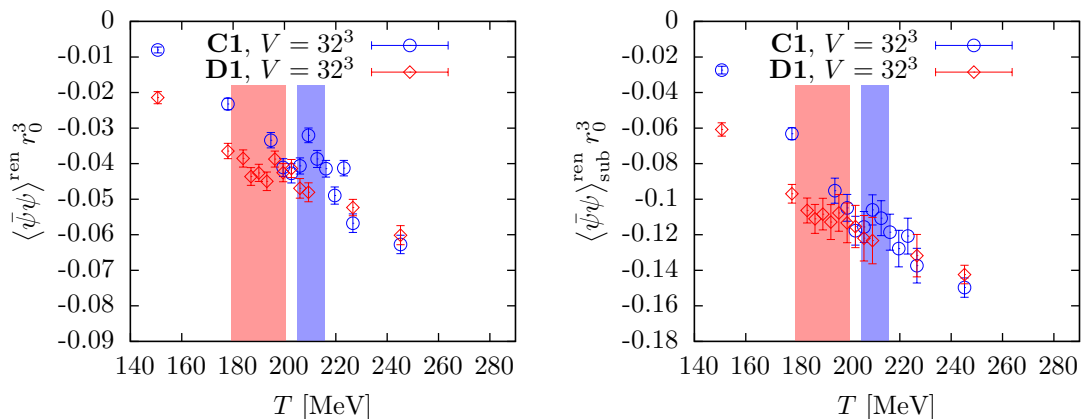


Figure 5. Results for the renormalised standard (left) and subtracted (right) condensate in scans **C1** and **D1**. The shaded areas display the estimates for T_C .

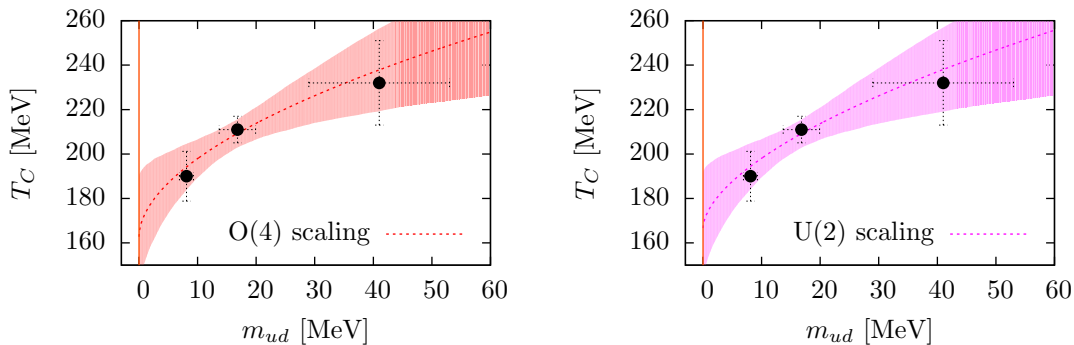


Figure 6. Results from the scaling fits to T_C using the critical exponents from the O(4) (left) and U(2) (right) scenarios.

analysis of the order parameter and its susceptibility (see [9]) might help in this respect. However, this would demand the knowledge of the scaling function from eq. (2.16) for the U(2) case. A distinction will only be possible if the scaling functions differ significantly.

In the first order scenario we also have to fix the value of the critical quark mass m_{ud}^{cr} . Since m_{ud}^{cr} is poorly constrained by the fit, we can try fits for different fixed values of m_{ud}^{cr} and look for minima in χ^2/dof . We find that, not unexpectedly, χ^2/dof is very flat and does not exhibit a minimum. Furthermore, χ^2/dof is always of the same order as for the second order fits. As a typical case we show the curve obtained for $m_{ud}^{\text{cr}} = 1.7$ MeV in figure 7. As for the scaling with the O(4) and U(2) critical exponents, the Z(2) curve agrees very well with the data and is hardly distinct from the curves of figure 6.

Obviously, none of the scenarios is ruled out by the above analysis. These findings are in agreement with the results from the tmfT collaboration [36]. When we assume that the data shows consistency with one of the second order scenarios and extract the associated

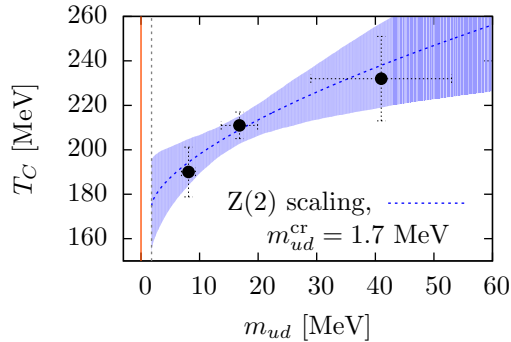


Figure 7. Results for the scaling fit for the first order scenario, i.e. the Z(2) universality class, with $m_{ud}^{\text{cr}} = 1.7$ MeV.

critical temperatures in the chiral limit we obtain

$$T_C(0)|_{\text{O}(4)} = 163(27) \text{ MeV} \quad \text{and} \quad T_C(0)|_{\text{U}(2)} = 167(25) \text{ MeV}. \quad (3.1)$$

Both results are consistent with the findings from the tmfT collaboration for O(4) scaling, $T_C(0) = 152(26)$ MeV [36], and are on the lower side of the results for Wilson fermions at $N_t = 4$, $T_C(0) = 171(4)$ MeV [33], and of the study of the QCDSF-DIK collaboration with different N_t values $T_C(0) = 172(7)$ MeV [35]. Calculations using staggered fermions only quote values for the critical coupling in the chiral limit, without providing results for the lattice spacing. The two results in eq. (3.1) indicate that the result for $T_C(0)$ is not sensitive to the universality class used for the extrapolation. This property is just another manifestation of the difficulty to distinguish between the two scenarios and shows that even a reduction of the error bars by an order of magnitude, in combination with results at much smaller quark masses, might not be sufficient using the scaling of the transition temperatures alone.

3.3 Screening masses and chiral symmetry restoration pattern

We now turn to the investigation of screening masses and the chiral symmetry restoration pattern. Since the behaviour of screening masses below and close to T_C in general depends on the quark mass we will focus on the scans along LCPs in this section, i.e. on scans **C1** and **D1**.

The screening correlators have been measured in the x_3 direction on the stored configurations using unsmearred point sources. To make efficient use of the generated configurations we have computed the correlation functions for 48 randomly chosen source positions (see also [64]). Compared to Ref. [58], we have thus enlarged the statistics by another factor of three. Screening masses are extracted from the effective mass ², aM_X^{eff} , defined by the

²Note, that the procedure differs from the one used in [62], where we have used a direct fit to the correlator. In general, the two sets of results are consistent within errors. The current set of measurements supersedes the ones from [62].

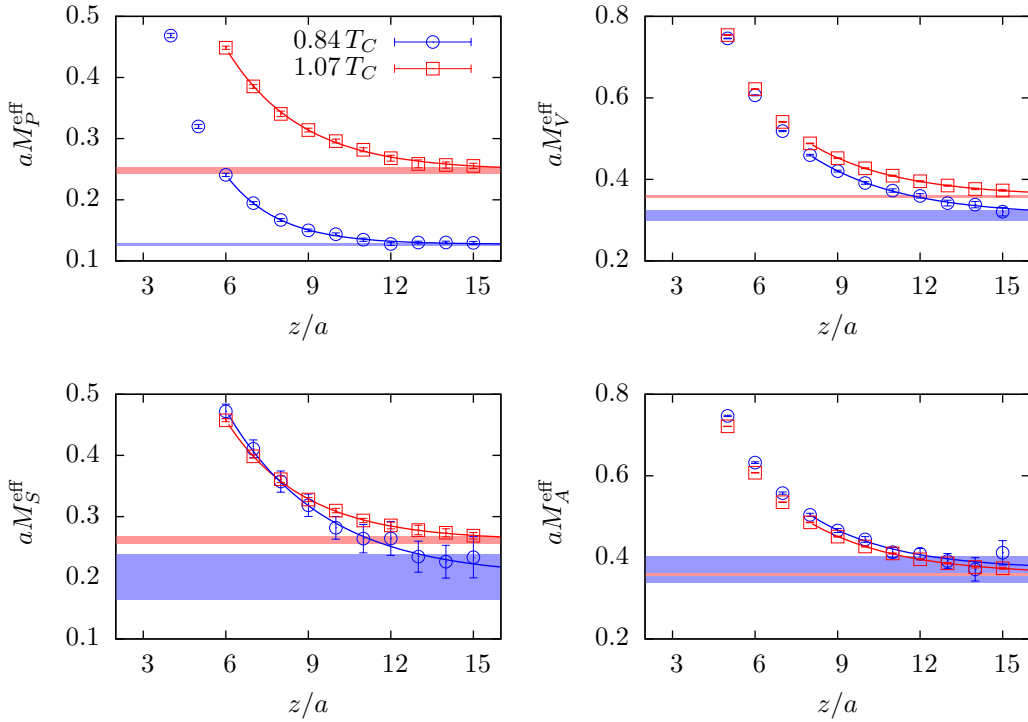


Figure 8. Effective masses for $T = 0.84$ and $1.07 T_C$ in P (top left), S (bottom left), V (top right) and A (bottom right) channels in lattice units from scan **C1**. The solid lines are the results from a constant plus exponential fit to the points that are within the area for which the curves are shown and the shaded area indicates the result for the effective mass.

formula for the inverse hyperbolic cosine,

$$aM_X^{\text{eff}}(z) = \ln \left[\frac{C(z+a) + C(z-a)}{2C(z)} + \sqrt{\left(\frac{C(z+a) + C(z-a)}{2C(z)} \right)^2 - 1} \right], \quad (3.2)$$

where $C = C_{XX}$. Since in scans **C1** and **D1** the spatial extent is rather small we could not find reasonable plateaus in most of the cases due to contaminations from excited states (see also [62]). To take the contaminations into account we have fitted the results for the effective mass to the form

$$aM_X^{\text{eff}}(z) = aM_X + aA \exp(-\Delta z), \quad (3.3)$$

where A and Δ are additional fit parameters. In figure 8 we show examples for the effective masses in the different channels above and below T_C , together with the results from the associated fits.

The formula for the effective mass follows to leading order when the contamination from the first excited state is included in the correlation function. In this case Δ represents the energy gap between groundstate and first excited state in this channel. However, when contaminations from higher excited states become important Δ (and A) will also contain

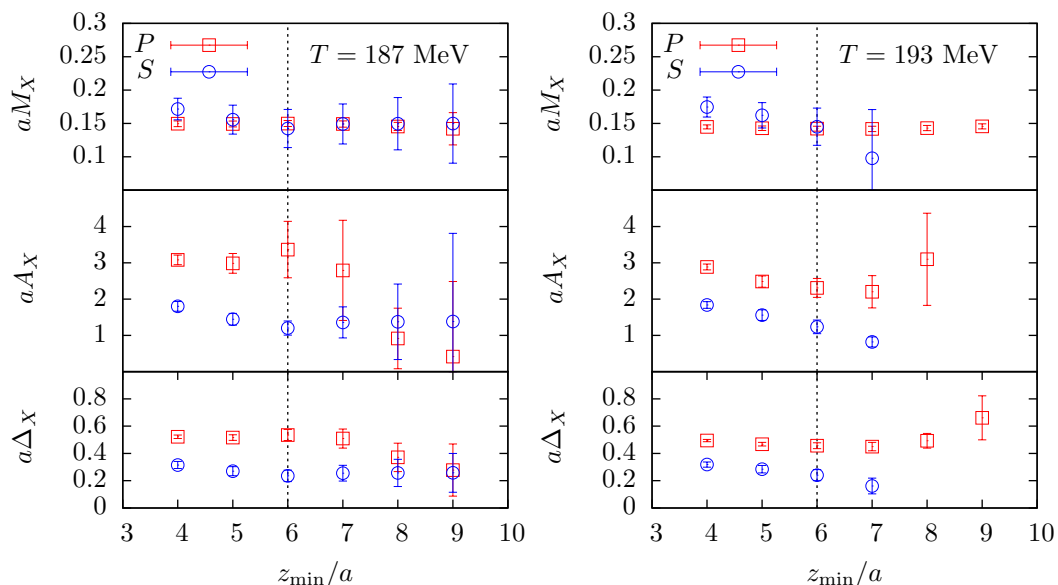


Figure 9. Result for the fit parameters of the fits for the extraction of screening masses versus the starting point z_{\min} of the fit. Shown are the results for the temperatures of 187 MeV (left) and 193 MeV (right) from scan **D1**. The vertical line corresponds to the choice for z_{\min} used to obtain the final results.

contributions from those. In both cases a fit to the form (3.3) is known to improve the extraction of the groundstate energy significantly and to remove most of the contaminations of the excited states. Note that neither A nor Δ are of direct importance for the following analysis. The fits to the form (3.3) typically work well for a variety of fitranges with starting points z_{\min} in the range from $4a$ to $9a$ for P and S channels and between $6a$ and $11a$ for V and A channels.³ In these regions the results for M_X do not depend significantly on the particular choice of fitrange and also the change of A and Δ is only significant in a few cases. We show the results for M_X , A and Δ from two representative cases in P and S channels close to the critical temperature for **D1** (where contaminations from excited states are typically expected to be most pronounced due to the small quark mass in the scan) in figure 9. Note, that the S channel is the more problematic one, both due to large statistical uncertainties and large contaminations from excited states (see also figures 8 and 12). In fact, the results shown in the right panel of figure 9 for the S channels are an example for the case where the fits do not work starting from $z_{\min}/a = 8$. Given these results, we conclude that for these values of z_{\min} the main contribution to Δ comes from the first excited state. Within these regions where the fitparameters are insensitive to the particular choice for z_{\min} we can choose to work with any value of z_{\min} . We decided to use $z_{\min} = 6a$ for P and S channels and $z_{\min} = 8a$ for V and A channels. For these values all

³For fits with yet larger z_{\min} the information in the data is not sufficient to constrain all three fit parameters sufficiently. In this case one could try a fit to a constant to extract M_X , but this procedure is less reliable than the use of eq. (3.3).

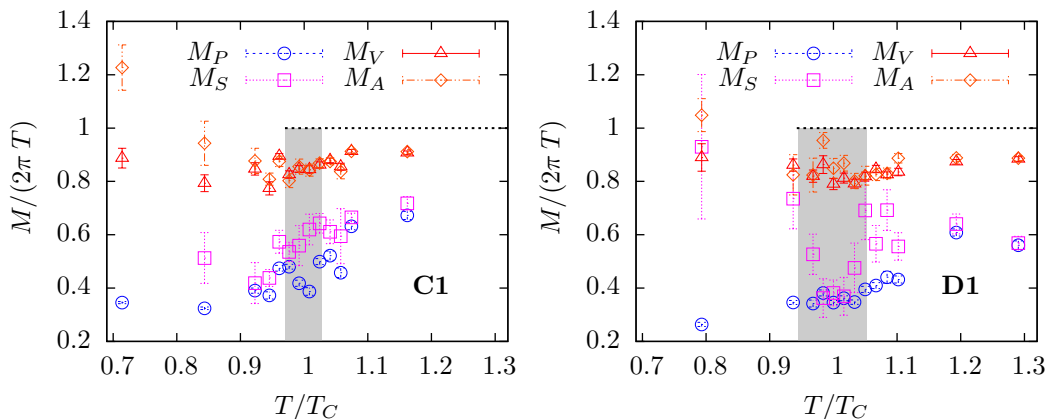


Figure 10. Results for the screening masses in the different channels for scans **C1** (left) and **D1** (right). The screening masses are normalised to the asymptotic limit M^∞ .

of the fits give a reasonable χ^2/dof around 1.⁴

The results for the screening masses are shown in figure 10. At $T/T_C \approx 0.7$ the screening masses show the expected splitting from the zero temperature meson masses [88]. While the masses in the P and V channels initially remain constant, indicated by a slight decrease of M/T , the screening masses in S and A channels decrease drastically in the approach to T_C . Around $T/T_C \approx 0.9$ all screening masses start to increase. In particular, the screening masses in P and S channels are drastically enhanced. Around T_C the screening masses in the V and A channels are mostly degenerate and around 85 to 90% of the asymptotic $2\pi T$ limit, independent of the quark mass in the scan. This is consistent with the findings in simulations with staggered fermions [89, 90].

The screening masses in P and S channels move closer together and fluctuate strongly around T_C . For the P channel the screening masses are only around 40 to 50% of the $2\pi T$ limit for scan **C1** with a pion mass of around 300 MeV and 35 to 40% for scan **D1** with a pion mass around 200 MeV, indicating a quark mass dependence of the properties of pseudoscalar (and scalar) states around T_C . The screening mass in the S channel is typically around 10% larger than M_P . In the temperature interval covered by our calculations above T_C , all screening masses are below the asymptotic high temperature limit. Note that weak-coupling calculations [93, 94] predict the asymptotic approach to occur from above, implying that the screening masses must cross the value $2\pi T$ at a certain temperature.

Our findings are in good agreement with the results for screening masses obtained with staggered fermions [89, 90]. In simulations within the quenched approximation, finite size effects have been found to be significant up to aspect ratios of $N_s/N_t = 4$ [105, 106]. To get an idea about their magnitude, we compare the effective masses in the different

⁴Note that there were a few cases for the S and A channels for $T < T_C$ where the fit ranges needed to be adapted due to large uncertainties for larger z values. However, those cases have no influence on the further analysis.

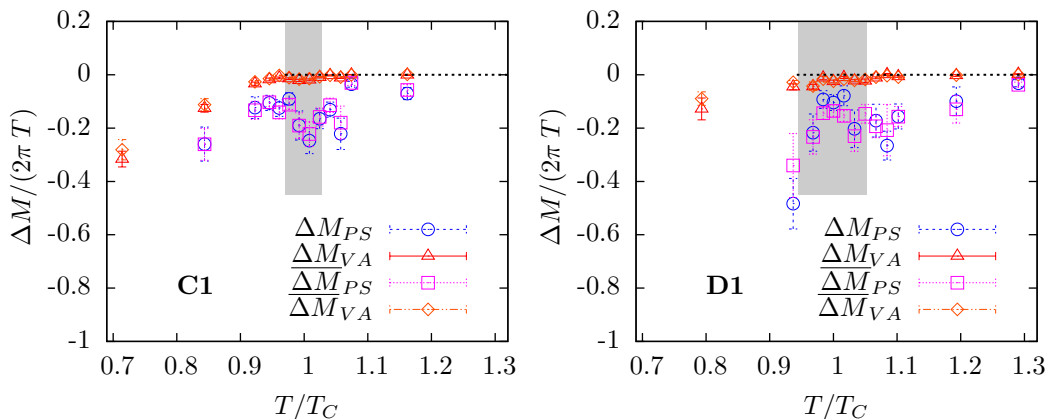


Figure 11. Results for the screening mass differences in the P and S channels, ΔM_{PS} , and in V and A channels, ΔM_{VA} , for scans **C1** (left) and **D1** (right). The differences are normalised to $2\pi T$.

channels at $T = 150$ MeV from scan **C1** (with a volume of 32^3) with those obtained from a simulation with the same parameters but an increased spatial volume of 48^3 . The comparison is shown in figure 12, no significant finite size effects are visible in the data. Note that the comparison is done for the lattice with the smallest value of $M_P L$ (which is the relevant quantity governing the size of finite volume effects in the confined phase) in the scan **C1**, being smaller than $M_P L$ for all simulation points in the transition region. We thus conclude that our final results are not strongly affected by finite size effects.

The chiral symmetry restoration pattern can be investigated by the degeneracies of the screening masses. To extract the differences,

$$\Delta M_{YX} = M_Y - M_X, \quad (3.4)$$

we have used the plateau in the effective masses of the ratios of the two correlation functions. In these ratios some of the fluctuations between different ensembles, evident in figure 10, and statistical fluctuations cancel. For these differences, some of the contaminations of the excited states cancel as well, so that we could use a fit to a constant, where we reduced the fitrange to the last few points. As for the fits to extract the screening masses, we have explicitly checked that our results do not depend significantly on the particular choice for the fitrange. This is in particular true when we consider that the main uncertainties in the following analysis are coming from the fluctuation between different ensembles in the region close to T_C . On top of these checks for the fits, we also checked the extraction of the mass splittings using a fit to the plateau in the ratio of effective masses M_X/M_Y to obtain another estimate for the difference via

$$\overline{\Delta M}_{YX} \equiv M_Y \left(\frac{M_X}{M_Y} - 1 \right). \quad (3.5)$$

In addition, we have also compared the results from the direct differences of screening masses. Note that in a very few cases the fit for ΔM_{PS} failed, and in one case this also happened within the transition region ($\beta = 5.37$ for scan **D1**). We have excluded this

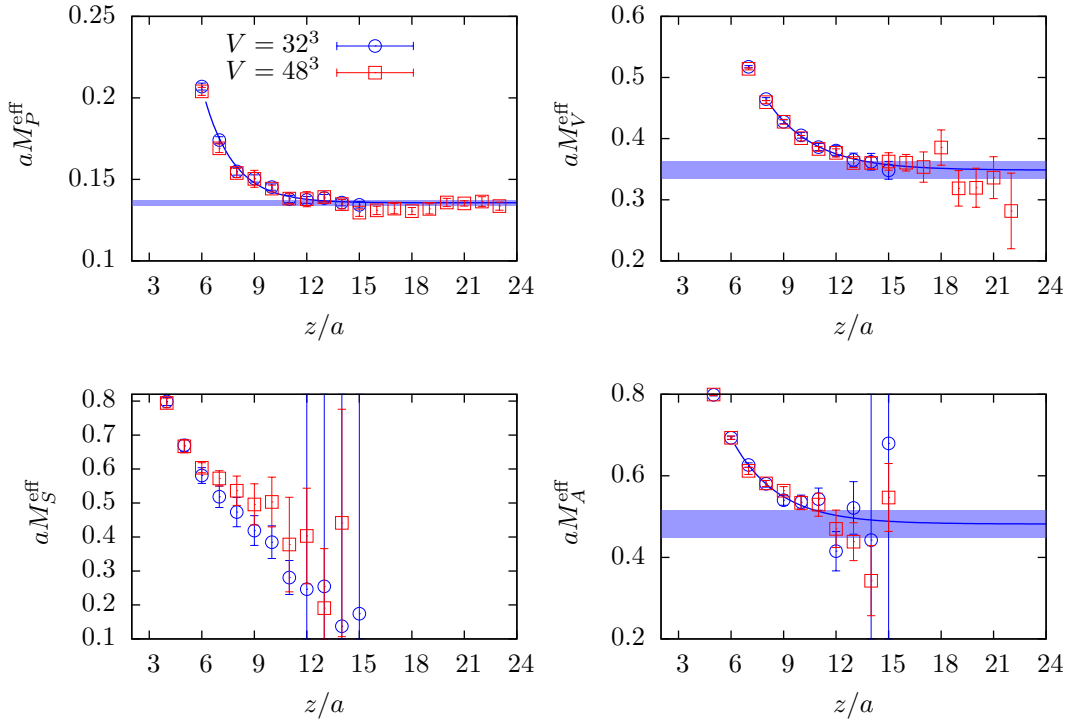


Figure 12. Effective masses for $T = 150$ MeV for scan **C1** with a 32^3 volume and for the future scan **C2** with a 48^3 volume. The solid lines are the results from a constant plus exponential fit to the points for scan **C1** that are within the area for which the curves are shown and the shaded area indicates the result for the effective mass. For the scalar screening masses the excited states fits did not work, so that we could not include any fit result in the plot.

datapoint from the following analysis, but we have checked with the mass difference of the independently determined screening masses that ΔM_{PS} for this β value indeed lies within the uncertainty of the final estimate.

In figure 11 we show the results for the mass differences. The plot indicates the degeneracy of M_V and M_A and the associated restoration of the $SU_A(2)$ symmetry around T_C for both scans. As already noted above, this is in agreement with the results from staggered fermion simulations [89, 90]. This also adds to the confidence concerning the extracted transition temperatures. In particular, both estimates for the mass difference agree very well over the whole temperature range for these channels (the ratio fit does not work for the lowest temperatures so that we have no reliable results in that region). For M_P and M_S there is still a significant mass splitting in the region around T_C , which, however, appears to become weaker with decreasing quark mass. For the following analysis we will conventionally use the direct results for the mass differences, i.e. the results labeled by ΔM_{XY} . The persistent mass splitting in P and S channels implies a residual breaking of $U_A(1)$ around T_C in agreement with what has been found with staggered [89], domain wall [10, 11, 107] and overlap [38, 39] fermion formulations. To make any statement about the fate and strength of the breaking in the chiral limit, however, we still need to perform

	B1_{κ}	C1	D1	$m_{ud} = 0$ linear	$m_{ud} = 0$ sqrt
ΔM_{PS} [MeV]	-272(33)(479)	-172(24)(158)	-121(23)(127)	-82(282)	5(590)

Table 5. Results for ΔM_{PS} at T_C for the different scans. The first error is statistical, the second reflects the systematic error owing to the fluctuations in the transition region. The value labeled with “ $m_{ud} = 0$ linear” is the result from the linear chiral extrapolation to all three points, as explained in the text, and the value labeled with “ $m_{ud} = 0$ sqrt” assumes a quark mass dependence proportional to $\sqrt{m_{ud}}$. The uncertainty on the result of the chiral extrapolations contains the statistical as well as the systematical uncertainty.

a chiral extrapolation, which is the topic of the next section.

3.4 On the relative size of the $U_A(1)$ breaking effects around T_C

An important question is which amount of symmetry breaking is “strong” or “weak”. When looking at the domain wall fermion results [10, 11] for chiral susceptibilities, one might be led to the conclusion that the breaking is significant in the chiral limit. The same is true if one looks at the eigenvalues of the associated Dirac operator [107]. However, the chiral susceptibilities include contributions from contact terms which might give an additional contribution that overwhelms the effect of chiral symmetry breaking. The eigenvalues are a more sensitive probe of the $U_A(1)$ breaking. In this case, studies with the overlap operator [38–40] have indicated that the residual breaking in the chiral limit might be weak in contrast to the breaking implied by the eigenvalues of the domain wall operator at finite extent of the fifth dimension.

In contrast to the studies discussed above, we use non-perturbatively $O(a)$ -improved Wilson fermions, which break chiral symmetry explicitly. The symmetry only becomes restored in the continuum limit. Since we use the mesonic screening spectrum as a probe, the results are expected to approach the continuum with $O(a^2)$ corrections. On our relatively fine lattices ($N_t = 16$), we expect these effects to be numerically small. We saw in the previous section that we do observe – to a good accuracy – the expected degeneracy between the vector and axial-vector screening above T_C , signalling the restoration of the non-anomalous chiral symmetry. Similarly, if the $U_A(1)$ symmetry becomes effectively restored, we expect to obtain $U_A(1)$ -breaking mass splittings of $O(a^2)$. In particular, since both the anomalous and the non-anomalous chiral symmetry are broken explicitly by the Wilson term, we expect the lattice artefacts to be of the same order of magnitude. Owing to the results for the difference between vector and axial-vector screening masses we expect this effect to contribute corrections of order 10 MeV. Furthermore, any accidental cancellation between lattice artefacts and a mass splitting in the continuum can only happen on this scale. Determining the strength of the breaking with a relative precision better than a few MeV requires taking the continuum limit.

We will now look at the chiral extrapolation of the mass difference ΔM_{PS} in physical units. First of all, using the value $m_{a0} = 980(20)$ MeV from the particle data group [108]

we obtain as an estimate for the zero temperature reference value at the physical point

$$\Delta M_{PS}^{T=0} = -845(20) \text{ MeV}. \quad (3.6)$$

This value might serve as an estimate for the effect in the mass difference when the breaking of $U_A(1)$ is substantial. However, this estimate is valid for physical, non-zero light quark mass, while we are interested in its value in the chiral limit. The pion mass vanishes in the chiral limit, so that $\Delta M_{PS}^{T=0, m_{ud}=0} = -m_{a0}^{m_{ud}=0}$. Next we need an estimate for $m_{a0}^{m_{ud}=0}$, for which we use the following ansatz: we assume that the difference between chiral limit and physical point is solely due to the change of the constituent quark masses m_q^{const} in the meson and compare with another “iso-vector” scalar particle in the review of the Particle Data Group (PDG) [109], namely the K_0^* , where one of the u/d quarks is replaced by a strange quark. This results in the ansatz

$$m_{a0} - m_{K_0^*} = C(m_{u,d}^{\text{const}} - m_s^{\text{const}}), \quad (3.7)$$

where C is a proportionality constant, which can be determined from eq. (3.7). Using C we can estimate the mass of the scalar in the chiral limit following

$$m_{a0} - m_{a0}^{m_{ud}=0} = 2Cm_{u,d}, \quad (3.8)$$

where the factor 2 comes from the fact that we need to send the masses of two quarks to zero. Using the numbers from the PDG [109] we obtain the final estimate $m_{a0}^{m_{ud}=0} = 945(41)$ MeV. The error estimate follows from the uncertainties associated with the masses of the $a0$ and the K_0^* mesons. This is a rather crude estimate, but it is unlikely that it underestimates the effect by an order of magnitude (even then $m_{a0}^{m_{ud}=0} \approx 600$ MeV, which does not change the picture dramatically). Our final estimate for the chiral limit is

$$\Delta M_{PS}^{T=0, m_{ud}=0} = -945(41) \text{ MeV}. \quad (3.9)$$

The width of the transition region must be taken into account when we extract an estimate for ΔM_{PS} from our simulations. We thus compute the difference from a fit to a constant to the data points in the grey bands in figure 11. The spread of the results in the region is taken as a systematic uncertainty on top of the statistical uncertainty of the average. The results from this procedure are listed in table 5. Here we have also included a result for scan $\mathbf{B1}_\kappa$ to be able to perform a sensible chiral extrapolation. Unfortunately, $\mathbf{B1}_\kappa$ is not at fixed quark mass and thus remains longer in the vicinity of T_C , since the latter increases with the quark mass. This accounts for the rather large error bars for the associated ΔM_{PS} .

To perform the chiral extrapolation for ΔM_{PS} we need to deduce its quark mass dependence. Since the pion is a Goldstone boson, its mass is expected to be proportional to $\sqrt{m_{ud}}$, at least at small temperatures, $T < T_C$. On the other hand, the mass of the scalar should depend linearly on the quark mass which might also be the case for the pion at T_C , where chiral perturbation theory breaks down. Given that we have only three data points at our disposal with relatively large uncertainties, our data clearly does not allow

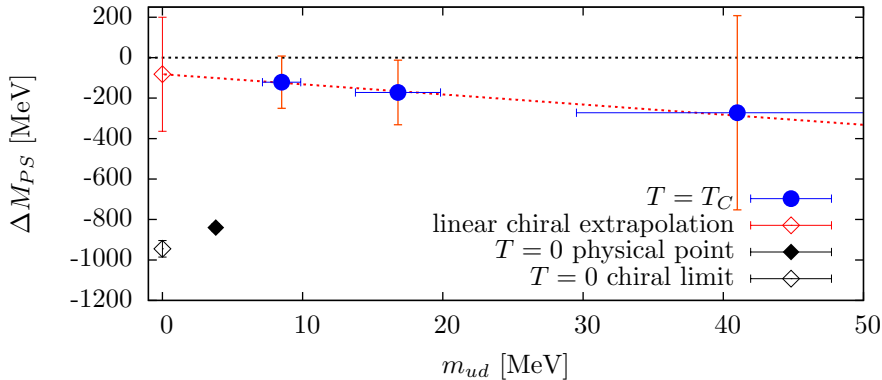


Figure 13. Chiral extrapolation of ΔM_{PS} in physical units in comparison to the zero temperature pendant estimated as explained in the text. The red line and the associated red point at $m_{ud} = 0$ indicate the result from a linear chiral extrapolation.

for a detailed investigation of the quark mass dependence of ΔM_{PS} . We thus perform two types of fits; (i) linear in m_{ud} , (ii) proportional to $\sqrt{m_{ud}}$. The results for the two different types of fits including all three data points are listed in table 5. We see that both results are consistent with zero within the relatively large error bars. As our final estimate we will thus use the linear fit. The associated result is shown in figure 13. We have also checked the robustness of the result with a linear fit using only the data from scans **C1** and **D1**. For this chiral extrapolation the central value remains within the error bar of the result quoted in table 5, but the uncertainty of the result increases.

Figure 13 indicates that the $U_A(1)$ -breaking screening-mass difference is a fairly small effect and has a mild quark-mass dependence only. In fact, at $m_{ud} = 0$ the breaking effects are strongly suppressed compared to the effect in the same quantity at zero temperature and consistent with zero. Our result is thus in qualitative agreement with the results from the spectrum of overlap fermions [39, 40].

4 Conclusions

In this paper we studied the finite temperature transition of two-flavour QCD on 16×32^3 (and 48^3) lattices. In particular, we have presented our results for the deconfinement and chiral symmetry restoration temperatures, extracted from the inflection point of the Polyakov loop and the peak in the susceptibility of the subtracted chiral condensate, respectively. In agreement with previous studies in the literature, we find both temperatures to decrease with the quark mass [26–36]. Our results for the chiral symmetry restoration temperatures, reported in table 4, are within uncertainties consistent with the values quoted by the tmfT collaboration [36, 110].

The ultimate goal of our ongoing efforts is to determine the order of the transition in the chiral limit. In an attempt to extract information about the chiral limit, we tested for scaling of the transition temperatures in the approach to the chiral limit. As already

reported in [58], the scaling behaviour alone is not sufficiently constrained to distinguish between a second order $O(4)$ chiral transition or a first order transition with a $Z(2)$ endpoint. This is consistent with earlier findings of the tmfT collaboration [36], even though we were able to reduce the pion masses in our study down to 200 MeV. Extrapolations of the critical temperatures to the chiral limit are not very sensitive to the universality class. Our results, when interpreted in terms of the $O(4)$ and $U(2)$ scenarios are consistent with the findings from the tmfT collaboration for $O(4)$ scaling [36], and somewhat smaller than those for Wilson fermions at $N_t = 4$ [33] and the QCDSF-DIK collaboration with different N_t values [35]. The fact that the chiral transition temperature does not appear to be very sensitive to the universality class used for the chiral extrapolation is one particular manifestation of the difficulty to distinguish between different scenarios. Even a reduction of the error bars by an order of magnitude in combination with results from smaller quark masses might not be sufficient to allow to distinguish between the universality classes when using the scaling of the transition temperatures alone.

As an alternative, we have investigated the strength of the anomalous breaking of the $U_A(1)$ symmetry in the chiral limit by computing the symmetry restoration pattern of screening masses in various isovector channels. At $T/T_C \approx 0.7$ the screening masses assume values close to the zero temperature meson masses. Initially the masses in the scalar and axial-vector channels decrease, before at $T/T_C \approx 0.9$ all masses start to increase. Around T_C the screening masses in the vector and axial-vector channels are degenerate and about 85 to 90% of the asymptotic $2\pi T$ limit, while the screening masses in the pseudoscalar channel are about 35 to 50% of this limit and exhibit a significant dependence on the quark mass. The screening mass in the scalar channel is typically around 10% larger. When going to higher temperatures all screening masses approach the $2\pi T$ limit from below, while leading-order weak-coupling calculations [93, 94] predict an asymptotic approach from above. All these findings are in qualitative agreement with the results found in $N_f = 2+1$ simulations with staggered fermions [89, 90].

To quantify the strength of the $U_A(1)$ -anomaly in the chiral limit, we use the difference between scalar and pseudoscalar screening masses, ΔM_{PS} . Unlike susceptibilities, screening masses probe exclusively the long distance properties of the correlation functions and thus do not suffer from contact terms. The comparison of the chirally extrapolated value, $\Delta M_{PS}^{m_{ud}=0} = -81(282)$ MeV to its zero temperature analogue $\Delta M_{PS}^{T=0, m_{ud}=0} = -945(41)$ MeV (cf. eq. (3.9)) suggests that the $U_A(1)$ -breaking is strongly reduced at the transition temperature (see also figure 13). If this effect persists in the continuum limit, it disfavors a chiral transition in the $O(4)$ universality class.

Acknowledgments

We thank our colleagues from CLS for the access to the zero-temperature ensembles. B.B. would like to thank Bastian Knippschild for sharing his routine for APE smearing and Gergely Endrődi for many helpful discussions. We acknowledge the use of computer time for the generation of the gauge configurations on the JURIPA, JUGENE and JUQUEEN computers of the Gauss Centre for Supercomputing at Forschungszentrum Jülich, allocated

through the John von Neumann Institute for Computing (NIC) within project HMZ21. The correlation functions and part of the configurations were computed on the dedicated QCD platforms “Wilson” at the Institute for Nuclear Physics, University of Mainz, and “Clover” at the Helmholtz-Institut Mainz. We also acknowledge computer time on the FUCHS cluster at the Centre for Scientific Computing of the University of Frankfurt. This work was supported by the *Center for Computational Sciences in Mainz* as part of the Rhineland-Palatine Research Initiative and by DFG grant ME 3622/2-1 *Static and dynamic properties of QCD at finite temperature*. B.B. has also received funding by the DFG via SFB/TRR 55 and the Emmy Noether Programme EN 1064/2-1.

A Simulation and analysis details

A.1 Simulation algorithms and associated constraints

The simulations have been done using the deflation accelerated versions of the Schwarz [67, 68] (DD) and mass [69, 70] (MP) preconditioned HMC algorithms. Both algorithms employ the Schwarz preconditioned and deflation accelerated generalised conjugate residual (DFL-SAP-GCR) solver introduced by Lüscher in [71, 72]. Due to the efficient solver, both algorithms exhibit an improved scaling behaviour when lowering the quark mass and the lattice spacing.

The block structures used in the solver and the preconditioning of the HMC algorithm impose constraints on the size of the local lattices allocated to the single processors. The main limitation follows from the constraint that Schwarz preconditioning blocks in the solver (SAP-blocks) have a minimal size of 4^4 [71]. At least two of these blocks need to fit into a sublattice, so that the minimal sublattice size when using a SAP solver is 8×4^3 . This restriction translates directly to the version of the MP-HMC algorithm from [70]. The restrictions for the sizes of the DD-blocks are essentially the same as for the SAP-blocks, but it also affects the efficiency of the HMC preconditioning, since the separation of modes works most efficiently if the DD-blocks have a minimal size of about half a fermi in each direction [67]. The inverse critical temperature corresponds to a temporal extent of about 1 fm, meaning that the size of the DD-blocks should be half the size of the temporal extent. For our scans the optimal sublattice size for the DD-HMC is thus given by 16×8^3 . Further constraints follow from the use of even/odd preconditioning in the different levels of the solver (see [71, 72] for the details). Summarizing, the algorithm restricts one to use lattice sizes of $N_{t/s} = 8, 12, 16, 20, \dots$

In our initial runs (see [59–61]) we used the DD-HMC algorithm. A drawback of the algorithm is that a sizeable fraction R of the links remain fixed during the molecular dynamics evolution [67]. While the ergodicity can be restored by shifting the gauge field between two HMC trajectories, the autocorrelation between two trajectories increases significantly. For typical block sizes of 4^4 and 8^4 one obtains $R = 0.09$ and 0.37 . For $N_t = 16$ the optimal block size is 8^4 , for which the autocorrelations are expected to be enhanced by about a factor of 3 compared to the MP-HMC algorithm. In particular on large scale machines, one is often forced to use a large number of processors and decrease the local

β	5.20	5.30	5.50
r_0/a	6.15(6)	7.26(7)	10.00(11)
κ_c	0.136055(4)	0.136457(4)	0.1367749(8)

Table 6. Input from zero temperature for scale setting and the estimation of LCPs taken from [74].

system size, meaning that autocorrelations increase drastically and the algorithm becomes inefficient. An example is the $\mathbf{B3}_\kappa$ lattice discussed in [58].

Due to the suppression of low modes above T_C accompanying the effective restoration of the chiral symmetry, the main motivation for using deflation gradually disappears. The reduced benefit of deflation can be observed in practice. However, for the lattices and quark masses in this study, there is still a significant acceleration even above T_C . In the region around and below T_C we had rare appearances of problems with deflation, most likely stemming from the fact that the “little” Dirac operator (see [72] for the details) has large condition numbers. Mostly these issues could be solved by changing the parameters of the deflation subspace.

A.2 Error analysis

For the error analysis we employ the bootstrap procedure [111] with 1000 bins. The data for different time slices of correlation functions is correlated, which means that in fits the full covariance matrix has to be taken into account. In practice, however, the uncertainties for the entries of the correlation matrix are often not precise enough for a stable least-square minimisation (see [112] for instance). This is in particular true for screening masses that typically have a bad signal-to-noise ratio. All our fits to correlation functions have thus neglected the non-diagonal terms of the correlation matrices.

For scale setting and renormalisation we have used interpolations of quantities that have their own uncertainties and for which we have no access to the raw data. To take these uncertainties into account, we have generated uncorrelated pseudo-bootstrap distributions with 1000 bins, whose width reproduces the quoted uncertainties. The interpolations have then been done for each bin, giving bins for the desired quantities at each value of the coupling.

A.3 Interpolation of zero temperature quantities

In this appendix we discuss the interpolations of several quantities, such as lattice spacing and quark masses. For scale setting we perform an interpolation of r_0/a obtained from the CLS lattices [74, 113], summarised in table 6. The final result is obtained using the ansatz [114]

$$\ln[a/r_0(\beta)] = c_0 + c_1\beta + c_2\beta^2, \quad (\text{A.1})$$

motivated by the solution of the renormalisation group equation for the bare coupling to two-loops. To check the model dependence of the result we use a simple polynomial of second order,

$$r_0/a(\beta) = \bar{c}_0 + \bar{c}_1\beta + \bar{c}_2\beta^2. \quad (\text{A.2})$$

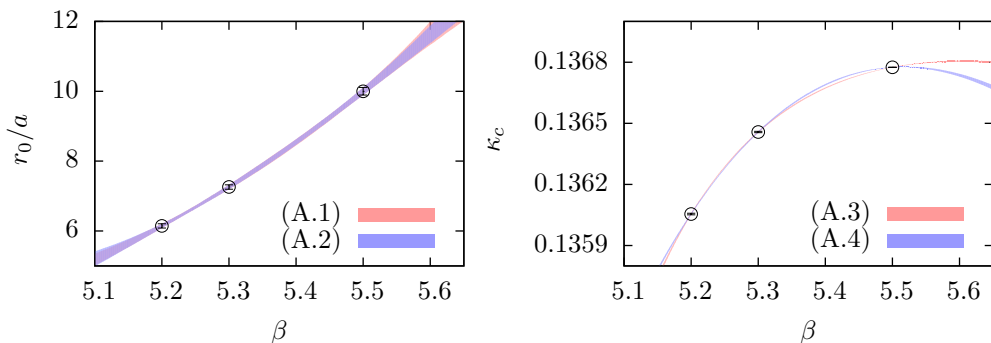


Figure 14. Interpolations of r_0/a (left) and κ_c (right).

The results for the coefficients are tabulated in table 7 and the interpolation is visualised in figure 14 (left). The plot displays the good agreement between the two interpolations, indicating that in the region $5.20 \leq \beta \leq 5.50$, systematic errors due to the ansatz for $r_0/a(\beta)$ are negligible.

Another important quantity is the critical hopping parameter κ_c . We interpolate the result from [74], listed in table 6, using the two different ansätze,

$$\kappa_c(\beta) = \frac{1}{8} \frac{1 + d_0/\beta + d_1/\beta^2}{1 + d_2/\beta}, \quad (\text{A.3})$$

$$\kappa_c(\beta) = \frac{1}{8} + \bar{d}_0/\beta + \bar{d}_1/\beta^2 + \bar{d}_2/\beta^3. \quad (\text{A.4})$$

The results are also listed in table 7 and the interpolations are shown in figure 14 (right). There is a slight model dependence in the region $5.35 \lesssim \beta \lesssim 5.45$. However, the interpolation mostly concerns the estimation of LCPs and does not enter the final analysis.

For the other renormalisation factors and improvement coefficients we have used known interpolation formulas from the literature: for Z_V we have used the interpolation formula from [115]; for c_A the one from [116]; for Z_A and Z_P we have used the results from [74]; for b_m and $[b_A - b_P]$ we have used the non-perturbative result from [117].

A.4 Estimating lines of constant physics

LCPs can be realised once we have an analytic relation between the bare parameter κ and the renormalised quark mass m_{ud} . This relation can be obtained by using the two different definitions for m_{ud} in the case of Wilson fermions. The first definition uses the bare quark mass \bar{m} [118],

$$m_{ud}^{\text{bare}} = Z_m (1 + b_m a\bar{m}) \bar{m} \quad \text{with} \quad a\bar{m} = \frac{1}{2} \left(\frac{1}{\kappa} - \frac{1}{\kappa_c} \right), \quad (\text{A.5})$$

where Z_m is the scheme dependent mass renormalisation factor and b_m is an $O(a)$ improvement coefficient. Another possibility is to use the PCAC quark mass [119],

$$m_{ud}^{\text{PCAC}} = \frac{Z_A}{Z_P} (1 + [b_A - b_P] a\bar{m}) m_{\text{PCAC}}. \quad (\text{A.6})$$

c_0	c_1	c_2		\bar{c}_0	\bar{c}_1	\bar{c}_2
-13(17)	3.9(62)	-0.21(58)		184(120)	-79(45)	8.6(42)
d_0	d_1	d_2		\bar{d}_0	\bar{d}_1	\bar{d}_2
-4.089(19)	-2.967(8)	-4.703(16)		-0.82(4)	10.2(4)	-29.0(9)
z_0	z_1	z_2	χ^2/dof			
55(37)	-20(14)	1.9(13)	0.2			

Table 7. Results of the fits for the interpolations of zero temperature results and the analytic relation $am_{\text{PCAC}}(\beta, \kappa)$. Note, that the for the interpolations there are as many parameters as data points, so that it is a parameterisation rather than a fit.

Here Z_A and Z_P are the renormalisation factors for the axial current and the pseudoscalar density (Z_P is scheme dependent) and b_A and b_P are due to improvement. m_{PCAC} is the bare quark mass defined by the PCAC relation (see [74, 77]).

Both quantities in eqs. (A.5) and (A.6) are estimates for the renormalized quark mass m_{ud} and differ only in lattice artifacts. From eqs. (A.5) and (A.6) we can thus infer (see also [117])

$$am_{\text{PCAC}} = Z_{\text{PCAC}}(\beta) (1 + [b_m + b_P - b_A] a\bar{m}) a\bar{m}. \quad (\text{A.7})$$

Eq. (A.7) is valid up to $O(a^2)$ corrections and $Z_{\text{PCAC}}(\beta)$ only depends on the regularisation scheme (i.e. the lattice discretisation), but not on the renormalisation scheme. Inserting the relation between $a\bar{m}$ and κ we obtain

$$am_{\text{PCAC}}(\beta, \kappa) = \frac{Z_{\text{PCAC}}(\beta)}{2} \left(\frac{1}{\kappa} - \frac{1}{\kappa_c(\beta)} \right) + Z_2(\beta) \left(\frac{1}{\kappa} - \frac{1}{\kappa_c(\beta)} \right)^2 + \dots \quad (\text{A.8})$$

For $\kappa_c(\beta)$ we take the known relation from appendix A.3. When m_{ud} is small $a\bar{m}$ is small as well. Since the factor Z_2 contains the combination of b -factors from eq. (A.7), which is dominated by b_m , and is a number smaller than one, we can expect that the second term in eq. (A.8) is negligible for small quark masses. We thus have to obtain only the β -dependence of the factor Z_{PCAC} . To this end we use the data for m_{PCAC} at $T = 0$ from [74, 77], listed in table 8. Since data is available only for three couplings, we will use a simple second order polynomial,

$$Z_{\text{PCAC}}(\beta) = z_0 + z_1\beta + z_2\beta^2. \quad (\text{A.9})$$

The fit with this ansatz works reasonably well, giving a small χ^2/dof of 0.2. In fact, χ^2/dof does not make any statements about the goodness of the ansatz for $Z_{\text{PCAC}}(\beta)$, but it shows that for the given range of quark masses am_{PCAC} and $a\bar{m}$ are indeed linearly related. The results for the coefficients z_i are listed in table 7. For renormalisation we can then use eq. (A.6) with the constants from appendix A.3 which are valid for the Schrödinger functional scheme. To convert to the $\overline{\text{MS}}$ scheme we use the conversion factor $m_{ud}^{\overline{\text{MS}}}/m_{ud}^{\text{SF}} = 0.968(20)$ [62, 77].

Note, that the final error bars on m_{ud} obtained from the relation $m_{ud}(\beta, \kappa)$ are much smaller than the uncertainties of the coefficients suggest, due to compensations of changes

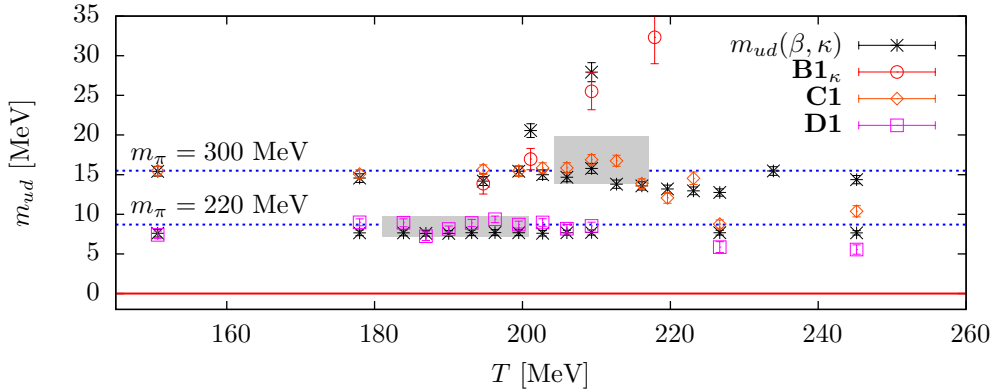


Figure 15. Comparison between $m_{ud}(\beta, \kappa)$ and the simulation results.

in one parameter by the others. Figure 15 shows a comparison between the predictions from $m_{ud}(\beta, \kappa)$ with the results obtained from the actual simulations. The plot displays the good agreement for temperatures below and up to T_C . Note, that the tuning for scan **C1** has been done using an early version of the matching with less information from the $T = 0$ side. This explains the fact that the black points do not lie on a constant m_{ud} line in that case. The good agreement between the measured quark masses and the predictions from the matching reported here indicates that this updated form of the matching works well. Above T_C , m_{ud} is typically lower than expected. It is unclear to us whether this result is an effect due to markedly different cutoff effects above T_C , or if the interpolation becomes worse at the higher β values. Note that our zero temperature ensembles are located at the β -values corresponding to 150, 180 and 245 MeV, so that the systematic error associated with the interpolation is expected to be most severe around 210 MeV.

A.5 Interpolation of the zero temperature chiral condensate

For the computation of the renormalised condensate the computation of the $T = 0$ subtraction terms is mandatory. Here we have computed $\langle \bar{\psi}\psi \rangle^{\text{bare}}$ and $\langle \overline{PP} \rangle$ on the CLS lattices, summarised with the measurement details in table 8. For the computation we have used $12 Z_2 \times Z_2$ volume (for $\langle \bar{\psi}\psi \rangle^{\text{bare}}$) and wall (for $\langle \overline{PP} \rangle$) sources on each configuration.

We have tested several different functional forms for the interpolation and found simple polynomials in $a\bar{m}$ to work best. Note, that $\langle \overline{PP} \rangle$ is expected to diverge linearly in $a\bar{m}$, since the condensate, which is finite at $a\bar{m} = 0$, is proportional to $\bar{m} \langle \overline{PP} \rangle$, which can be described by a polynomial. We have thus used

$$\begin{aligned} a^3 \langle \bar{\psi}\psi \rangle^{\text{bare}}(\beta, \kappa) &= p_1(\beta) + p_2(\beta)(2a\bar{m}) + p_3(\beta)(2a\bar{m})^2 \\ a^3 \langle \overline{PP} \rangle(\beta, \kappa) &= \bar{p}_1(\beta)/(2a\bar{m}) + \bar{p}_2(\beta) + \bar{p}_3(\beta)(2a\bar{m}), \end{aligned} \quad (\text{A.10})$$

with

$$p_i(\beta) = q_1^i + q_2^i \beta + q_3^i \beta^2 \quad (\text{A.11})$$

β	κ	size	# config	am_{PCAC}	$a^3 \langle \bar{\psi}\psi \rangle^{\text{bare}}$	$a^3 \langle \overline{PP} \rangle$
5.20	0.13565	64×32^3	289	0.0158(2)	0.2727633(18)	0.2064(1)
	0.13580		265	0.0098 (3)	0.2727369(19)	0.2203(2)
	0.13590		400	0.0057 (4)	0.2727055(15)	0.2428(5)
	0.13594		211	0.0044 (2)	0.2726914(23)	0.2609(10)
	0.13597	96×48^3	400		0.2726827(7)	0.2878(9)
5.30	0.13610	64×32^3	162		0.2711093(16)	0.1883(1)
	0.13625		508	0.0072 (3)	0.2711386(11)	0.2004(2)
	0.13635			0.00375(11)		
	0.13638	96×48^3	250	0.00267(9)	0.2711641(9)	0.2438(7)
	0.13642	128×64^3	205		0.2711734(5)	0.3162(22)
5.50	0.13650	96×48^3	83	0.0091 (2)	0.2685038(8)	0.1645(1)
	0.13660		188	0.0059 (2)	0.2685683(6)	0.1702(1)
	0.13667		221	0.00343(12)	0.2686063(5)	0.1782(2)
	0.13671	128×64^3	137	0.00213(6)	0.2686293(5)	0.1912(3)

Table 8. Set of CLS $T = 0$ lattices used for the determination of the relation $m_{ud}(\beta, \kappa)$ and the computation of the condensate at zero temperature and the associated results. For the measurements of am_{PCAC} and more details on the lattices we refer to [74, 77].

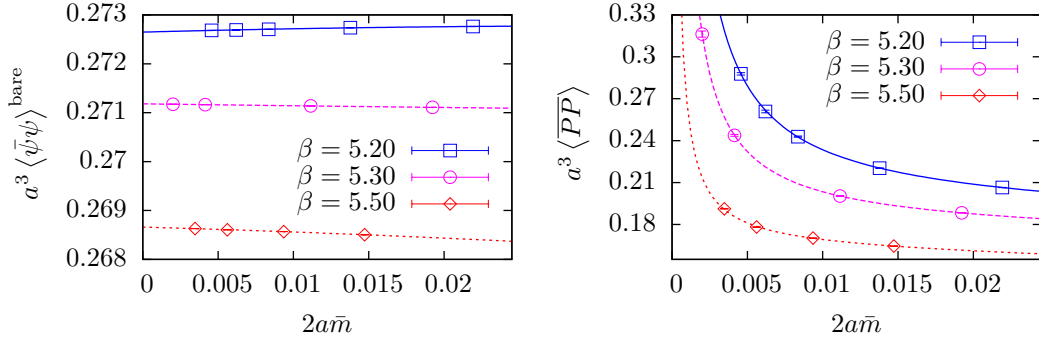


Figure 16. Interpolation of the results for the bare (left) and subtracted (right) condensates obtained on the CLS lattices, as described in the text.

(similarly for \bar{p}_i with $q \rightarrow \bar{q}$) and as usual $2a\bar{m} = 1/\kappa - 1/\kappa_c(\beta)$ with $\kappa_c(\beta)$ obtained from the standard interpolation (A.3). Altogether, each fit has 9 fit parameters. The results are given in table 9 and the interpolations for the different β -values are shown in figure 16. The χ^2/dof values are 3.3 and 5.5 for $\langle \bar{\psi}\psi \rangle^{\text{bare}}$ and $\langle \overline{PP} \rangle$, respectively. The tiny error bars on $\langle \bar{\psi}\psi \rangle^{\text{bare}}$ and $\langle \overline{PP} \rangle$ explain the bad values for χ^2/dof , despite the fit providing a satisfactory description of the data. Once more, the uncertainties of the fit parameters do not reflect the uncertainty on the results for the condensate. Note that we have neglected finite volume effects for the condensates, which appears to be justified for $m_\pi L \gtrsim 4$.

B Simulation parameters and results

q_1^1	q_2^1	q_3^1	q_1^2	q_2^2	q_3^2	q_1^3	q_2^3	q_3^3
0.539(4)	-0.087(2)	0.0069(2)	9.6(8)	-3.5(3)	0.32(3)	-207(34)	77(13)	-7.2(12)
\bar{q}_1^1	\bar{q}_2^1	\bar{q}_3^1	\bar{q}_1^2	\bar{q}_2^2	\bar{q}_3^2	\bar{q}_1^3	\bar{q}_2^3	\bar{q}_3^3
0.084(49)	-0.030(19)	0.0027(17)	6.1(55)	-2.1(21)	0.19(19)	-80(170)	30(64)	-2.8(60)

Table 9. Results for the fit parameters for the interpolation of the chiral condensate at $T = 0$.

Scan	β	κ	MDU	T [MeV]	m_{ud} [MeV]	τ_{U_p} [MDU]
B1$_{\kappa}$	5.375	0.136500	10000	201(5)	17.0(1.4)	26(5)
	5.400		22000	209(5)	25.5(2.4)	56(8)
	5.425		20200	218(5)	32.3(3.4)	32(4)
	5.450		20600	227(5)	39.6(2.0)	20(2)
	5.475		21600	236(5)	39.3(2.0)	22(3)
	5.48125		20200	238(5)	46.2(2.2)	18(2)
	5.4875		19600	240(6)	46.9(2.1)	21(3)
	5.49375		21400	243(6)	45.3(2.1)	19(3)
	5.496875		16200	244(6)	47.9(2.2)	16(2)
	5.500		21600	245(6)	45.5(2.0)	19(2)
	5.503125		16600	246(6)	43.6(2.1)	16(2)
	5.50625		21000	248(6)	49.7(2.5)	17(2)
	5.5125		21600	250(6)	47.7(2.4)	17(2)
	5.51875		19800	252(6)	50.6(2.2)	14(2)
	5.525		19400	255(6)	53.5(2.5)	17(2)
5.550		19200	265(7)	51.3(2.4)	14(2)	
5.575		12200	275(8)	55.6(2.7)	13(2)	
C1	5.20	0.135940	12320	151(4)	15.5(6)	96(28)
	5.30	0.136356	12260	178(4)	15.1(6)	24(3)
	5.355	0.136500	13040	195(5)	15.6(7)	34(7)
	5.37	0.136523	12560	199(5)	15.5(7)	19(3)
	5.38	0.136545	12240	203(5)	15.8(7)	25(4)
	5.39	0.136565	12240	206(5)	15.9(7)	20(3)
	5.40	0.136575	12080	209(5)	16.9(7)	24(5)
	5.41	0.136603	12320	213(5)	16.8(7)	31(5)
	5.42	0.136619	12080	216(5)	13.9(7)	23(4)
	5.43	0.136635	12480	220(5)	12.1(7)	22(4)
	5.44	0.136649	12166	223(5)	14.5(8)	15(2)
	5.45	0.136662	12000	227(5)	8.8(6)	15(2)
	5.50	0.136700	12480	245(6)	10.4(8)	14(2)
	D1	5.20	0.135998	4800	151(4)	7.4(5)
5.30		0.136404	8600	178(4)	9.0(6)	12(2)
5.32		0.136460	8040	185(4)	8.9(5)	10(2)
5.33		0.136486	12000	187(4)	7.2(6)	14(3)
5.34		0.136510	14280	190(4)	8.1(4)	14(2)
5.35		0.136532	14320	193(5)	8.9(5)	16(3)
5.36		0.136553	14200	196(5)	9.4(4)	9(1)
5.37		0.136573	13440	199(5)	8.7(5)	9(2)
5.38		0.136592	10520	203(5)	9.0(5)	9(2)
5.39		0.136609	8200	206(5)	8.2(6)	9(2)
5.40		0.136625	8440	209(5)	8.5(5)	8(1)
5.45		0.136691	8560	227(5)	5.9(7)	8(2)
5.50		0.136735	7840	245(6)	5.6(6)	5(1)

Table 10. Run parameters of the simulations. We list the bare lattice coupling β , the hopping parameter κ , the number of molecular dynamics units (MDU), temperature, renormalised quark mass in the $\overline{\text{MS}}$ -scheme at a renormalisation scale of 2 GeV and the autocorrelation time of the plaquette (τ_{U_p}).

T [MeV]	$\langle L \rangle$ $\cdot 10^4$	$\langle L_S \rangle$ $\cdot 10^2$	$\langle \bar{\psi}\psi \rangle^{\text{bare}}$	$\bar{\chi}_{\langle \bar{\psi}\psi \rangle}^{\text{bare}}$ $\cdot r_0^2$	$\langle \bar{\psi}\psi \rangle^{\text{ren}}$ $\cdot r_0^3 \cdot 10^2$	$\langle \bar{\psi}\psi \rangle_{\text{sub}}^{\text{bare}}$	$\bar{\chi}_{\langle \bar{\psi}\psi \rangle_{\text{sub}}}^{\text{bare}}$ $\cdot r_0^2$	$\langle \bar{\psi}\psi \rangle_{\text{sub}}^{\text{ren}}$ $\cdot r_0^3 \cdot 10^2$
B1_κ								
201	4.6(6)	3.1(3)						
209	5.1(5)	2.8(2)						
218	6.8(4)	3.7(3)	0.269397(9)	0.28(9)	-2.5(7)	0.1691(13)	0.47(10)	-7.2(1.3)
227	6.9(4)	4.0(2)	0.269085(6)	0.21(5)	-1.8(5)	0.1649(6)	0.52(11)	-8.0(9)
236	10.0(4)	5.6(2)	0.268751(6)	0.24(6)	-4.5(6)	0.1592(5)	0.27(11)	-12.9(8)
238	9.3(6)	5.0(3)						
249	8.7(3)	4.7(2)	0.268614(7)	0.21(5)	-3.6(7)	0.1598(6)	0.44(10)	-10.5(1.1)
243	9.9(6)	5.3(3)	0.268534(5)	0.22(5)	-4.3(5)	0.1584(5)	0.46(16)	-12.3(9)
244	10.2(6)	5.4(3)						
245	9.9(7)	5.3(3)	0.268459(7)	0.23(7)	-4.8(8)	0.1586(7)	0.42(6)	-11.3(1.3)
246	11.3(5)	6.1(2)						
248	11.3(4)	5.9(2)	0.268378(6)	0.13(4)	-5.9(7)	0.1568(4)	0.19(5)	-14.1(9)
250	11.5(3)	6.0(2)	0.268304(8)	0.18(4)	-6.5(9)	0.1570(5)	0.33(10)	-13.0(1.1)
252	11.5(4)	6.1(2)						
255	12.9(3)	6.5(2)	0.268156(4)	0.12(4)	-8.0(6)	0.1551(3)	0.15(3)	-16.1(1.0)
265	13.5(5)	6.9(2)	0.267863(3)	0.16(6)	-12.5(10)	0.1527(1)	0.04(2)	-20.7(1.4)
275	15.9(4)	7.7(2)	0.267589(4)	0.11(7)	-17.2(18)	0.1515(1)	0.08(3)	-23.9(2.1)
C1								
151	0.7(4)	0.59(3)	0.272657(4)	0.38(3)	-0.8(9)	0.2849(8)	2.23(20)	-2.7(3)
178	2.0(4)	1.21(4)	0.271101(3)	0.34(3)	-2.3(2)	0.2050(7)	1.05(9)	-6.3(4)
195	4.9(3)	2.76(6)	0.270331(3)	0.31(2)	-3.3(3)	0.1831(5)	0.59(7)	-9.5(7)
199	4.8(4)	2.76(6)	0.270120(3)	0.24(2)	-4.1(3)	0.1769(4)	0.33(4)	-10.5(8)
203	5.7(4)	3.52(6)	0.269991(3)	0.29(3)	-4.3(3)	0.1723(4)	0.26(4)	-11.8(9)
206	5.7(4)	3.45(6)	0.269869(2)	0.21(2)	-4.1(3)	0.1716(3)	0.20(3)	-11.6(9)
209	5.4(4)	3.40(6)	0.269754(3)	0.24(2)	-3.2(2)	0.1724(4)	0.33(4)	-10.6(9)
213	5.5(4)	3.31(8)	0.269627(3)	0.29(2)	-3.9(3)	0.1709(5)	0.35(4)	-11.1(10)
216	6.9(4)	3.85(6)	0.269503(2)	0.21(2)	-4.1(3)	0.1679(3)	0.15(2)	-11.9(11)
220	7.8(4)	4.49(7)	0.269375(2)	0.16(2)	-4.9(3)	0.1646(3)	0.09(2)	-12.8(11)
223	8.1(4)	4.80(7)	0.269267(2)	0.22(2)	-4.1(3)	0.1657(4)	0.20(3)	-12.1(11)
227	9.7(4)	5.38(6)	0.269133(2)	0.13(2)	-5.7(3)	0.1608(1)	0.01(1)	-13.7(10)
245	11.6(4)	6.21(7)	0.268564(2)	0.15(2)	-6.3(3)	0.1574(3)	0.09(4)	-15.0(6)
D1								
151	0.8(7)	0.89(6)	0.2725611(11)	0.64(8)	-2.1(2)	0.2859(50)	3.89(76)	-6.1(4)
178	2.5(4)	1.89(6)	0.2710744(4)	0.43(4)	-3.6(3)	0.2068(17)	1.54(32)	-9.7(6)
185	3.3(3)	2.15(6)	0.2708011(4)	0.37(3)	-3.9(3)	0.1963(11)	0.67(12)	-10.6(7)
187	3.1(3)	2.47(6)	0.2706568(3)	0.35(3)	-4.4(3)	0.1909(10)	0.71(15)	-11.1(9)
190	3.4(3)	2.36(5)	0.2705272(3)	0.37(3)	-4.3(3)	0.1901(10)	0.93(29)	-10.8(9)
193	4.0(3)	2.78(5)	0.2703920(2)	0.33(2)	-4.5(3)	0.1850(9)	0.69(16)	-11.3(10)
196	4.1(3)	2.86(5)	0.2702744(3)	0.32(3)	-3.9(3)	0.1858(11)	0.83(27)	-10.8(11)
199	4.7(3)	2.98(5)	0.2701396(2)	0.30(2)	-4.3(3)	0.1807(7)	0.42(7)	-11.3(12)
203	4.9(3)	3.14(6)	0.2700152(3)	0.29(2)	-4.1(3)	0.1778(7)	0.28(5)	-11.5(12)
206	5.4(4)	4.54(7)	0.2698810(3)	0.24(2)	-4.7(3)	0.1727(7)	0.27(13)	-12.2(13)
209	6.5(3)	3.96(7)	0.2697557(3)	0.23(2)	-4.8(3)	0.1705(6)	0.16(4)	-12.3(13)
227	8.5(4)	4.93(8)	0.2691539(2)	0.15(2)	-5.2(3)	0.1619(3)	0.02(7)	-13.2(12)
245	10.8(4)	5.85(9)	0.2685848(2)	0.15(2)	-6.0(3)	0.1580(2)	0.02(5)	-14.2(6)

Table 11. Simulation results for the (smeared) real part of the Polyakov loop, the bare chiral condensate and its disconnected susceptibility ($\langle \bar{\psi}\psi \rangle^{\text{bare}}$ and $\bar{\chi}_{\langle \bar{\psi}\psi \rangle}^{\text{bare}}$), the associated renormalised condensate ($\langle \bar{\psi}\psi \rangle^{\text{ren}}$) in units of r_0 , and the subtracted versions ($\langle \bar{\psi}\psi \rangle_{\text{sub}}^{\text{bare}}$, $\bar{\chi}_{\langle \bar{\psi}\psi \rangle_{\text{sub}}}^{\text{bare}}$ and $\langle \bar{\psi}\psi \rangle_{\text{sub}}^{\text{ren}}$).

T [MeV]	aM_P	aM_S	aM_V	aM_A	$a\Delta M_{PS}$	$a\Delta M_{VA} \cdot 10^2$
C1						
151	0.136(2)	—	0.348(15)	0.482(35)	—	-12.42(12)
178	0.127(2)	0.201(38)	0.311(13)	0.370(33)	-0.102(25)	-4.94(56)
195	0.153(4)	0.164(31)	0.332(9)	0.344(19)	-0.048(16)	-1.32(24)
199	0.146(6)	0.172(13)	0.304(10)	0.317(9)	-0.041(11)	-0.70(21)
203	0.186(5)	0.225(17)	0.351(4)	0.344(8)	-0.049(13)	-0.47(13)
206	0.189(4)	0.210(15)	0.324(6)	0.315(11)	-0.036(9)	-0.57(12)
209	0.164(5)	0.220(30)	0.332(5)	0.336(11)	-0.075(22)	-0.84(17)
213	0.152(6)	0.243(23)	0.332(6)	0.331(9)	-0.097(20)	-0.76(14)
216	0.196(5)	0.252(15)	0.338(5)	0.341(7)	-0.065(15)	-0.38(11)
220	0.205(7)	0.240(18)	0.345(4)	0.343(5)	-0.051(12)	-0.96(9)
223	0.180(7)	0.234(41)	0.336(6)	0.329(11)	-0.087(23)	-0.45(11)
227	0.248(6)	0.261(7)	0.359(3)	0.358(4)	-0.014(5)	0.01(3)
245	0.264(6)	0.282(10)	0.356(3)	0.358(3)	-0.028(9)	-0.03(3)
D1						
151	0.104(3)	0.365(107)	0.349(21)	0.412(25)	—	-5.0(1.7)
178	0.136(3)	0.289(45)	0.338(10)	0.324(30)	-0.190(38)	-1.8(5)
185	0.134(5)	0.207(30)	0.322(9)	0.323(25)	-0.086(28)	-1.8(4)
187	0.150(5)	0.142(29)	0.339(14)	0.375(12)	-0.037(13)	-0.5(3)
190	0.136(4)	0.150(19)	0.310(9)	0.333(15)	-0.041(12)	-1.0(3)
193	0.142(4)	0.145(28)	0.319(8)	0.342(12)	-0.031(15)	-0.4(2)
196	0.136(4)	0.186(37)	0.311(7)	0.315(12)	-0.080(28)	-0.9(2)
199	0.155(5)	0.271(44)	0.321(7)	0.323(14)	—	-0.9(3)
203	0.161(5)	0.222(27)	0.332(6)	0.324(9)	-0.068(24)	-0.5(2)
206	0.173(9)	0.272(30)	0.324(4)	0.326(8)	-0.104(22)	0.0(2)
209	0.170(6)	0.218(21)	0.328(6)	0.349(7)	-0.061(19)	-0.3(2)
227	0.239(6)	0.251(15)	0.343(4)	0.349(5)	-0.039(21)	-0.1(2)
245	0.220(7)	0.223(10)	0.347(4)	0.348(4)	-0.012(6)	0.1(1)

Table 12. Simulation results for screening masses M in P , S , V and A channels and the direct measurements for screening mass differences ΔM . The results for scan **B1** $_{\kappa}$ are not listed.

References

- [1] N. Brambilla et al., *QCD and Strongly Coupled Gauge Theories: Challenges and Perspectives*, *Eur. Phys. J.* **C74** (2014) 2981, [[1404.3723](#)].
- [2] K. Szabo, *QCD at non-zero temperature and magnetic field*, *PoS LATTICE2013* (2014) 014, [[1401.4192](#)].
- [3] H.-T. Ding, F. Karsch and S. Mukherjee, *Thermodynamics of strong-interaction matter from Lattice QCD*, [1504.05274](#).
- [4] A. Bazavov, *Lattice QCD at Non-Zero Temperature*, *PoS LATTICE2014* (2015) 392.
- [5] H. B. Meyer, *QCD at non-zero temperature from the lattice*, in *Proceedings, 33rd International Symposium on Lattice Field Theory (Lattice 2015)*, 2015. [1512.06634](#).
- [6] L. G. Yaffe and B. Svetitsky, *First Order Phase Transition in the SU(3) Gauge Theory at Finite Temperature*, *Phys. Rev.* **D26** (1982) 963.
- [7] R. D. Pisarski and F. Wilczek, *Remarks on the Chiral Phase Transition in Chromodynamics*, *Phys. Rev.* **D29** (1984) 338–341.
- [8] Y. Aoki, G. Endrődi, Z. Fodor, S. Katz and K. Szabo, *The Order of the quantum chromodynamics transition predicted by the standard model of particle physics*, *Nature* **443** (2006) 675–678, [[hep-lat/0611014](#)].
- [9] A. Bazavov, T. Bhattacharya, M. Cheng, C. DeTar, H. Ding et al., *The chiral and deconfinement aspects of the QCD transition*, *Phys.Rev.* **D85** (2012) 054503, [[1111.1710](#)].
- [10] HOTQCD collaboration, A. Bazavov et al., *The chiral transition and $U(1)_A$ symmetry restoration from lattice QCD using Domain Wall Fermions*, *Phys.Rev.* **D86** (2012) 094503, [[1205.3535](#)].
- [11] T. Bhattacharya, M. I. Buchoff, N. H. Christ, H.-T. Ding, R. Gupta et al., *QCD Phase Transition with Chiral Quarks and Physical Quark Masses*, *Phys.Rev.Lett.* **113** (2014) 082001, [[1402.5175](#)].
- [12] WHOT-QCD COLLABORATION collaboration, T. Umeda et al., *Equation of state in 2+1 flavor QCD with improved Wilson quarks by the fixed scale approach*, *Phys.Rev.* **D85** (2012) 094508, [[1202.4719](#)].
- [13] S. Borsanyi, S. Dür, Z. Fodor, C. Hoelbling, S. D. Katz et al., *QCD thermodynamics with continuum extrapolated Wilson fermions I*, *JHEP* **1208** (2012) 126, [[1205.0440](#)].
- [14] S. Borsanyi, S. Dür, Z. Fodor, C. Holbling, S. D. Katz, S. Krieg et al., *QCD thermodynamics with continuum extrapolated Wilson fermions II*, *Phys. Rev.* **D92** (2015) 014505, [[1504.03676](#)].
- [15] T. Umeda, S. Ejiri, R. Iwami and K. Kanaya, *Towards the QCD equation of state at the physical point using Wilson fermion*, in *Proceedings, 33rd International Symposium on Lattice Field Theory (Lattice 2015)*, 2015. [1511.04649](#).
- [16] F. Karsch, E. Laermann and C. Schmidt, *The Chiral critical point in three-flavor QCD*, *Phys.Lett.* **B520** (2001) 41–49, [[hep-lat/0107020](#)].
- [17] P. de Forcrand and O. Philipsen, *The Chiral critical line of $N(f) = 2+1$ QCD at zero and non-zero baryon density*, *JHEP* **01** (2007) 077, [[hep-lat/0607017](#)].

- [18] WHOT-QCD collaboration, H. Saito, S. Ejiri, S. Aoki, T. Hatsuda, K. Kanaya, Y. Maezawa et al., *Phase structure of finite temperature QCD in the heavy quark region*, *Phys. Rev.* **D84** (2011) 054502, [[1106.0974](#)].
- [19] M. Fromm, J. Langelage, S. Lottini and O. Philipsen, *The QCD deconfinement transition for heavy quarks and all baryon chemical potentials*, *JHEP* **01** (2012) 042, [[1111.4953](#)].
- [20] P. de Forcrand, S. Kim and O. Philipsen, *A QCD chiral critical point at small chemical potential: Is it there or not?*, *PoS LAT2007* (2007) 178, [[0711.0262](#)].
- [21] G. Endrődi, Z. Fodor, S. D. Katz and K. K. Szabo, *The Nature of the finite temperature QCD transition as a function of the quark masses*, *PoS LAT2007* (2007) 182, [[0710.0998](#)].
- [22] H. T. Ding, A. Bazavov, P. Hegde, F. Karsch, S. Mukherjee and P. Petreczky, *Exploring phase diagram of $N_f = 3$ QCD at $\mu = 0$ with HISQ fermions*, *PoS LATTICE2011* (2011) 191, [[1111.0185](#)].
- [23] X.-Y. Jin, Y. Kuramashi, Y. Nakamura, S. Takeda and A. Ukawa, *Critical endpoint of the finite temperature phase transition for three flavor QCD*, *Phys. Rev.* **D91** (2015) 014508, [[1411.7461](#)].
- [24] A. Butti, A. Pelissetto and E. Vicari, *On the nature of the finite temperature transition in QCD*, *JHEP* **08** (2003) 029, [[hep-ph/0307036](#)].
- [25] A. Pelissetto and E. Vicari, *Relevance of the axial anomaly at the finite-temperature chiral transition in QCD*, *Phys.Rev.* **D88** (2013) 105018, [[1309.5446](#)].
- [26] F. Karsch, *Scaling of pseudocritical couplings in two flavor QCD*, *Phys.Rev.* **D49** (1994) 3791–3794, [[hep-lat/9309022](#)].
- [27] F. Karsch and E. Laermann, *Susceptibilities, the specific heat and a cumulant in two flavor QCD*, *Phys. Rev.* **D50** (1994) 6954–6962, [[hep-lat/9406008](#)].
- [28] JLQCD collaboration, S. Aoki et al., *Scaling study of the two flavor chiral phase transition with the Kogut-Susskind quark action in lattice QCD*, *Phys. Rev.* **D57** (1998) 3910–3922, [[hep-lat/9710048](#)].
- [29] MILC collaboration, C. W. Bernard, T. Burch, T. A. DeGrand, C. E. Detar, S. A. Gottlieb, U. M. Heller et al., *Scaling tests of the improved Kogut-Susskind quark action*, *Phys. Rev.* **D61** (2000) 111502, [[hep-lat/9912018](#)].
- [30] M. D’Elia, A. Di Giacomo and C. Pica, *Two flavor QCD and confinement*, *Phys.Rev.* **D72** (2005) 114510, [[hep-lat/0503030](#)].
- [31] G. Cossu, M. D’Elia, A. Di Giacomo and C. Pica, *Two flavor QCD and confinement. II.*, [0706.4470](#).
- [32] C. Bonati, G. Cossu, M. D’Elia, A. Di Giacomo and C. Pica, *A Test of first order scaling in $N_f = 2$ QCD: A Progress report*, *PoS LATTICE2008* (2008) 204, [[0901.3231](#)].
- [33] CP-PACS COLLABORATION collaboration, A. Ali Khan et al., *Phase structure and critical temperature of two flavor QCD with renormalization group improved gauge action and clover improved Wilson quark action*, *Phys.Rev.* **D63** (2001) 034502, [[hep-lat/0008011](#)].
- [34] V. Bornyakov, R. Horsley, S. Morozov, Y. Nakamura, M. Polikarpov et al., *Probing the finite temperature phase transition with $N(f) = 2$ nonperturbatively improved Wilson fermions*, *Phys.Rev.* **D82** (2010) 014504, [[0910.2392](#)].

- [35] V. G. Bornyakov, R. Horsley, Y. Nakamura, M. I. Polikarpov, P. Rakow and G. Schierholz, *Finite temperature phase transition with two flavors of improved Wilson fermions*, *PoS LATTICE2010* (2014) 170, [[1102.4461](#)].
- [36] TMFT collaboration, F. Burger et al., *Thermal QCD transition with two flavors of twisted mass fermions*, *Phys.Rev.* **D87** (2013) 074508, [[1102.4530](#)].
- [37] TWQCD collaboration, T.-W. Chiu, W.-P. Chen, Y.-C. Chen, H.-Y. Chou and T.-H. Hsieh, *Chiral symmetry and axial $U(1)$ symmetry in finite temperature QCD with domain-wall fermion*, *PoS LATTICE2013* (2014) 165, [[1311.6220](#)].
- [38] G. Cossu, S. Aoki, H. Fukaya, S. Hashimoto, T. Kaneko et al., *Finite temperature study of the axial $U(1)$ symmetry on the lattice with overlap fermion formulation*, *Phys.Rev.* **D87** (2013) 114514, [[1304.6145](#)].
- [39] A. Tomiya, G. Cossu, H. Fukaya, S. Hashimoto and J. Noaki, *Effects of near-zero Dirac eigenmodes on axial $U(1)$ symmetry at finite temperature*, [1412.7306](#).
- [40] JLQCD collaboration, G. Cossu, H. Fukaya, S. Hashimoto, J.-i. Noaki and A. Tomiya, *On the axial $U(1)$ symmetry at finite temperature*, in *Proceedings, 33rd International Symposium on Lattice Field Theory (Lattice 2015)*, 2015. [1511.05691](#).
- [41] P. de Forcrand and O. Philipsen, *Constraining the QCD phase diagram by tricritical lines at imaginary chemical potential*, *Phys. Rev. Lett.* **105** (2010) 152001, [[1004.3144](#)].
- [42] C. Bonati, P. de Forcrand, M. D’Elia, O. Philipsen and F. Sanfilippo, *Chiral phase transition in two-flavor QCD from an imaginary chemical potential*, *Phys. Rev.* **D90** (2014) 074030, [[1408.5086](#)].
- [43] C. Pinke and O. Philipsen, *The $N_f = 2$ chiral phase transition from imaginary chemical potential with Wilson Fermions*, in *Proceedings, 33rd International Symposium on Lattice Field Theory (Lattice 2015)*, 2015. [1508.07725](#).
- [44] S. Ejiri and N. Yamada, *End Point of a First-Order Phase Transition in Many-Flavor Lattice QCD at Finite Temperature and Density*, *Phys. Rev. Lett.* **110** (2013) 172001, [[1212.5899](#)].
- [45] S. Ejiri, R. Iwami and N. Yamada, *Exploring the nature of chiral phase transition in two-flavor QCD using extra heavy quarks*, [1511.06126](#).
- [46] S. Aoki, H. Fukaya and Y. Taniguchi, *1st or 2nd the order of finite temperature phase transition of $N_f = 2$ QCD from effective theory analysis*, *PoS LATTICE2013* (2014) 139, [[1312.1417](#)].
- [47] JLQCD collaboration, S. Aoki, *Axial $U(1)$ symmetry in the chiral symmetric phase of 2-flavor QCD at finite temperature*, *PoS CD15* (2016) 045, [[1603.00997](#)].
- [48] G. V. Dunne and A. Kovner, *$U_A(1)$ Anomaly at high temperature: the scalar-pseudoscalar splitting in QCD*, *Phys. Rev.* **D82** (2010) 065014, [[1004.1075](#)].
- [49] T. D. Cohen, *The High temperature phase of QCD and $U(1)$ -A symmetry*, *Phys. Rev.* **D54** (1996) R1867–R1870, [[hep-ph/9601216](#)].
- [50] T. D. Cohen, *The Spectral density of the Dirac operator above $T(c)$ rep*, in *Properties of hadrons in matter. Proceedings, APCTP Workshop on astro-hadron physics, Seoul, Korea, October 25-31, 1997*, pp. 100–114, 1997. [nucl-th/9801061](#).

- [51] N. J. Evans, S. D. H. Hsu and M. Schwetz, *Topological charge and $U(1)$ -A symmetry in the high temperature phase of QCD*, *Phys. Lett.* **B375** (1996) 262–266, [[hep-ph/9601361](#)].
- [52] S. H. Lee and T. Hatsuda, *U - $a(1)$ symmetry restoration in QCD with $N(f)$ flavors*, *Phys. Rev.* **D54** (1996) R1871–R1873, [[hep-ph/9601373](#)].
- [53] S. Aoki, H. Fukaya and Y. Taniguchi, *Chiral symmetry restoration, eigenvalue density of Dirac operator and axial $U(1)$ anomaly at finite temperature*, *Phys. Rev.* **D86** (2012) 114512, [[1209.2061](#)].
- [54] V. Dick, F. Karsch, E. Laermann, S. Mukherjee and S. Sharma, *Microscopic origin of $U_A(1)$ symmetry violation in the high temperature phase of QCD*, *Phys. Rev.* **D91** (2015) 094504, [[1502.06190](#)].
- [55] M. I. Buchoff et al., *QCD chiral transition, $U(1)A$ symmetry and the dirac spectrum using domain wall fermions*, *Phys. Rev.* **D89** (2014) 054514, [[1309.4149](#)].
- [56] B. Sheikholeslami and R. Wohlert, *Improved Continuum Limit Lattice Action for QCD with Wilson Fermions*, *Nucl.Phys.* **B259** (1985) 572.
- [57] K. G. Wilson, *Confinement of Quarks*, *Phys.Rev.* **D10** (1974) 2445–2459.
- [58] B. B. Brandt, A. Francis, H. B. Meyer, O. Philipsen and H. Wittig, *QCD thermodynamics with $O(a)$ improved Wilson fermions at $N_f=2$* , [1310.8326](#).
- [59] B. B. Brandt, H. Wittig, O. Philipsen and L. Zeidlewicz, *Towards the $N_f = 2$ deconfinement transition temperature with $O(a)$ improved Wilson fermions*, *PoS LATTICE2010* (2010) 172, [[1008.2143](#)].
- [60] B. B. Brandt, O. Philipsen, H. Wittig and L. Zeidlewicz, *Towards the $N_f = 2$ deconfinement transition temperature with $O(a)$ improved Wilson fermions: An update*, *AIP Conf.Proc.* **1343** (2011) 516–518, [[1011.6172](#)].
- [61] B. B. Brandt, A. Francis, H. B. Meyer, H. Wittig and O. Philipsen, *QCD thermodynamics with two flavours of Wilson fermions on large lattices*, *PoS LATTICE2012* (2012) 073, [[1210.6972](#)].
- [62] B. B. Brandt, A. Francis, H. B. Meyer and D. Robaina, *Chiral dynamics in the low-temperature phase of QCD*, *Phys. Rev.* **D90** (2014) 054509, [[1406.5602](#)].
- [63] B. B. Brandt, A. Francis, H. B. Meyer and D. Robaina, *Chiral dynamics in the low-temperature phase of QCD*, *PoS LATTICE2014* (2015) 234, [[1410.5981](#)].
- [64] B. B. Brandt, A. Francis, H. B. Meyer and D. Robaina, *The pion quasiparticle in the low-temperature phase of QCD*, [1506.05732](#).
- [65] B. B. Brandt, A. Francis, H. B. Meyer and D. Robaina, *The pion quasiparticle in the low-temperature phase of QCD*, in *8th International Workshop on Chiral Dynamics (CD 2015) Pisa, Italy, June 29-July 3, 2015*, 2015. [1509.06241](#).
- [66] ALPHA COLLABORATION collaboration, K. Jansen and R. Sommer, *$O(\alpha)$ improvement of lattice QCD with two flavors of Wilson quarks*, *Nucl.Phys.* **B530** (1998) 185–203, [[hep-lat/9803017](#)].
- [67] M. Lüscher, *Schwarz-preconditioned HMC algorithm for two-flavour lattice QCD*, *Comput.Phys.Commun.* **165** (2005) 199–220, [[hep-lat/0409106](#)].
- [68] M. Lüscher, *Deflation acceleration of lattice QCD simulations*, *JHEP* **0712** (2007) 011, [[0710.5417](#)].

- [69] M. Hasenbusch, *Speeding up the hybrid Monte Carlo algorithm for dynamical fermions*, *Phys.Lett.* **B519** (2001) 177–182, [[hep-lat/0107019](#)].
- [70] M. Marinkovic and S. Schaefer, *Comparison of the mass preconditioned HMC and the DD-HMC algorithm for two-flavour QCD*, *PoS LATTICE2010* (2010) 031, [[1011.0911](#)].
- [71] M. Lüscher, *Solution of the Dirac equation in lattice QCD using a domain decomposition method*, *Comput.Phys.Commun.* **156** (2004) 209–220, [[hep-lat/0310048](#)].
- [72] M. Lüscher, *Local coherence and deflation of the low quark modes in lattice QCD*, *JHEP* **0707** (2007) 081, [[0706.2298](#)].
- [73] B. B. Brandt, A. Francis, B. Jäger and H. B. Meyer, *Charge transport and vector meson dissociation across the thermal phase transition in lattice QCD with two light quark flavors*, [1512.07249](#).
- [74] P. Fritzsche, F. Knechtli, B. Leder, M. Marinkovic, S. Schaefer et al., *The strange quark mass and Lambda parameter of two flavor QCD*, *Nucl.Phys.* **B865** (2012) 397–429, [[1205.5380](#)].
- [75] R. Sommer, *A New way to set the energy scale in lattice gauge theories and its applications to the static force and alpha-s in SU(2) Yang-Mills theory*, *Nucl.Phys.* **B411** (1994) 839–854, [[hep-lat/9310022](#)].
- [76] J. Bijnens, G. Colangelo and P. Talavera, *The Vector and scalar form-factors of the pion to two loops*, *JHEP* **9805** (1998) 014, [[hep-ph/9805389](#)].
- [77] B. B. Brandt, A. Jüttner and H. Wittig, *The pion vector form factor from lattice QCD and NNLO chiral perturbation theory*, *JHEP* **1311** (2013) 034, [[1306.2916](#)].
- [78] H. Wittig, *Improved Computational Methods for Monte Carlo Simulations of the SU(2) Higgs Model*, *Nucl.Phys.* **B325** (1989) 242.
- [79] APE collaboration, M. Albanese et al., *Glueball Masses and String Tension in Lattice QCD*, *Phys. Lett.* **B192** (1987) 163–169.
- [80] O. Kaczmarek, F. Karsch, P. Petreczky and F. Zantow, *Heavy quark anti-quark free energy and the renormalized Polyakov loop*, *Phys.Lett.* **B543** (2002) 41–47, [[hep-lat/0207002](#)].
- [81] G. Aarts, C. Allton, A. Amato, P. Giudice, S. Hands et al., *Electrical conductivity and charge diffusion in thermal QCD from the lattice*, [1412.6411](#).
- [82] L. H. Karsten and J. Smit, *Lattice Fermions: Species Doubling, Chiral Invariance, and the Triangle Anomaly*, *Nucl.Phys.* **B183** (1981) 103.
- [83] M. Bochicchio, L. Maiani, G. Martinelli, G. C. Rossi and M. Testa, *Chiral Symmetry on the Lattice with Wilson Fermions*, *Nucl.Phys.* **B262** (1985) 331.
- [84] L. Giusti, F. Rapuano, M. Talevi and A. Vladikas, *The QCD chiral condensate from the lattice*, *Nucl.Phys.* **B538** (1999) 249–277, [[hep-lat/9807014](#)].
- [85] C. E. Detar and J. B. Kogut, *The Hadronic Spectrum of the Quark Plasma*, *Phys.Rev.Lett.* **59** (1987) 399.
- [86] C. E. Detar and J. B. Kogut, *Measuring the Hadronic Spectrum of the Quark Plasma*, *Phys.Rev.* **D36** (1987) 2828.
- [87] H. B. Meyer, *Transport Properties of the Quark-Gluon Plasma: A Lattice QCD Perspective*, *Eur.Phys.J.* **A47** (2011) 86, [[1104.3708](#)].

- [88] F. Karsch and E. Laermann, *Thermodynamics and in medium hadron properties from lattice QCD*, [hep-lat/0305025](#).
- [89] M. Cheng, S. Datta, A. Francis, J. van der Heide, C. Jung et al., *Meson screening masses from lattice QCD with two light and the strange quark*, *Eur.Phys.J.* **C71** (2011) 1564, [[1010.1216](#)].
- [90] D. Banerjee, R. V. Gavai and S. Gupta, *Quasi-static probes of the QCD plasma*, *Phys.Rev.* **D83** (2011) 074510, [[1102.4465](#)].
- [91] V. Eletsky and B. Ioffe, *On Temperature Dependence of Correlators of Hadronic Currents*, *Sov.J.Nucl.Phys.* **48** (1988) 384.
- [92] W. Florkowski and B. L. Friman, *Spatial dependence of the finite temperature meson correlation function*, *Z.Phys.* **A347** (1994) 271–276.
- [93] M. Laine and M. Vepsalainen, *Mesonic correlation lengths in high temperature QCD*, *JHEP* **0402** (2004) 004, [[hep-ph/0311268](#)].
- [94] W. Alberico, A. Beraudo, A. Czerska, P. Czerski and A. Molinari, *Meson Screening Masses in the Interacting QCD Plasma*, *Nucl.Phys.* **A792** (2007) 152–169, [[hep-ph/0703298](#)].
- [95] B. Brandt, A. Francis, M. Laine and H. Meyer, *A relation between screening masses and real-time rates*, *JHEP* **1405** (2014) 117, [[1404.2404](#)].
- [96] B. Brandt, A. Francis, M. Laine and H. Meyer, *Vector screening masses in the quarkgluon plasma and their physical significance*, *Nucl.Phys.* **A931** (2014) 861–866, [[1408.5917](#)].
- [97] A. Pelissetto and E. Vicari, *Critical phenomena and renormalization group theory*, *Phys.Rept.* **368** (2002) 549–727, [[cond-mat/0012164](#)].
- [98] S. Ejiri, F. Karsch, E. Laermann, C. Miao, S. Mukherjee et al., *On the magnetic equation of state in (2+1)-flavor QCD*, *Phys.Rev.* **D80** (2009) 094505, [[0909.5122](#)].
- [99] K. Kanaya and S. Kaya, *Critical exponents of a three dimensional $O(4)$ spin model*, *Phys.Rev.* **D51** (1995) 2404–2410, [[hep-lat/9409001](#)].
- [100] Y. Nakayama, *Determining the order of chiral phase transition in QCD from conformal bootstrap*, *PoS LATTICE2015* (2016) 002.
- [101] S. Chandrasekharan and A. C. Mehta, *Effects of the anomaly on the two-flavor QCD chiral phase transition*, *Phys. Rev. Lett.* **99** (2007) 142004, [[0705.0617](#)].
- [102] ETM collaboration, K. Jansen, C. Michael and C. Urbach, *The eta-prime meson from lattice QCD*, *Eur. Phys. J.* **C58** (2008) 261–269, [[0804.3871](#)].
- [103] ETM collaboration, K. Jansen, C. McNeile, C. Michael and C. Urbach, *Meson masses and decay constants from unquenched lattice QCD*, *Phys. Rev.* **D80** (2009) 054510, [[0906.4720](#)].
- [104] B. B. Brandt, A. Francis and H. B. Meyer, *Antiscreening of the Ampere force in QED and QCD plasmas*, *Phys.Rev.* **D89** (2014) 034506, [[1310.5160](#)].
- [105] S. Wissel, E. Laermann, S. Shcheredin, S. Datta and F. Karsch, *Meson correlation functions at high temperatures*, *PoS LAT2005* (2006) 164, [[hep-lat/0510031](#)].
- [106] M. Müller, *parallel talk at lattice 2013*, .
- [107] JLQCD collaboration, G. Cossu et al., *Axial $U(1)$ symmetry at finite temperature with Möbius domain-wall fermions*, [1412.5703](#).

- [108] PARTICLE DATA GROUP collaboration, K. Olive et al., *Review of Particle Physics*, *Chin.Phys.* **C38** (2014) 090001.
- [109] PARTICLE DATA GROUP collaboration, C. Patrignani et al., *Review of Particle Physics*, *Chin. Phys.* **C40** (2016) 100001.
- [110] TMFT collaboration, F. Burger, E.-M. Ilgenfritz, M. P. Lombardo and M. Müller-Preussker, *Equation of state of quark-gluon matter from lattice QCD with two flavors of twisted mass Wilson fermions*, *Phys. Rev.* **D91** (2015) 074504, [[1412.6748](#)].
- [111] B. Efron, *Bootstrap methods: another look at the jackknife*, *Ann. Statist.* **7** (1979) 1–26.
- [112] C. Michael, *Fitting correlated data*, *Phys.Rev.* **D49** (1994) 2616–2619, [[hep-lat/9310026](#)].
- [113] ALPHA COLLABORATION collaboration, B. Leder and F. Knechtli, *Scale r_0 and the static potential from the CLS lattices*, *PoS LATTICE2010* (2010) 233, [[1012.1141](#)].
- [114] ALPHA COLLABORATION collaboration, M. Guagnelli, R. Sommer and H. Wittig, *Precision computation of a low-energy reference scale in quenched lattice QCD*, *Nucl.Phys.* **B535** (1998) 389–402, [[hep-lat/9806005](#)].
- [115] M. Della Morte, R. Hoffmann, F. Knechtli, R. Sommer and U. Wolff, *Non-perturbative renormalization of the axial current with dynamical Wilson fermions*, *JHEP* **0507** (2005) 007, [[hep-lat/0505026](#)].
- [116] M. Della Morte, R. Hoffmann and R. Sommer, *Non-perturbative improvement of the axial current for dynamical Wilson fermions*, *JHEP* **0503** (2005) 029, [[hep-lat/0503003](#)].
- [117] P. Fritzsche, J. Heitger and N. Tantalo, *Non-perturbative improvement of quark mass renormalization in two-flavour lattice QCD*, *JHEP* **1008** (2010) 074, [[1004.3978](#)].
- [118] M. Lüscher, S. Sint, R. Sommer and P. Weisz, *Chiral symmetry and $O(a)$ improvement in lattice QCD*, *Nucl.Phys.* **B478** (1996) 365–400, [[hep-lat/9605038](#)].
- [119] M. Lüscher, S. Sint, R. Sommer, P. Weisz and U. Wolff, *Nonperturbative $O(a)$ improvement of lattice QCD*, *Nucl.Phys.* **B491** (1997) 323–343, [[hep-lat/9609035](#)].